Theoretical and Applied Fracture Mechanics 127 (2023) 104029

Contents lists available at ScienceDirect

Theoretical and Applied Fracture Mechanics

journal homepage: www.elsevier.com/locate/tafmec

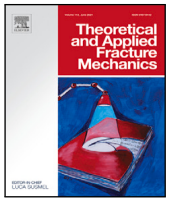

A phase-field fracture model for fatigue using locking-free solid shell finite elements: Analysis for homogeneous materials and layered composites

Pavan Kumar Asur Vijaya Kumar [a,b,*], Aamir Dean [c,d], José Reinoso [e], Heinz E. Pettermann [a], Marco Paggi [b]

[a] Institut für Leichtbau und Struktur-Biomechanik, Technische Universität Wien, Getreidemarkt 9, 1060 Vienna, Austria
[b] IMT School for Advanced Studies Lucca, Piazza San Francesco 19, 55100, Lucca, Italy
[c] School of Civil Engineering, College of Engineering, Sudan University of Science and Technology, P.O. Box 72, Khartoum, Sudan
[d] Institute of Structural Analysis, Leibniz Universität Hannover, Appelstr. 9A, 30167 Hannover, Germany
[e] Departamento de Mecánica de Medios Continuos y Teoría de Estructuras, School of Engineering, Universidad de Sevilla, Camino de los Descubrimientos s/n, 41092, Seville, Spain

ARTICLE INFO

Dataset link: https://github.com/Pavan-asur/Fatigue-Solidshell

Keywords:
A. Phase-field method
B. Solid-shell
C. Finite element method
D: Fatigue
E. Fracture

ABSTRACT

A computational framework to model fatigue fracture in structures based on the phase-field method and the solid-shell concept is herein presented. With the aim of achieving a locking free solid-shell finite element formulation with fracture-prediction capabilities, both the combination of the Enhanced Assumed Strain (EAS) and Assumed Natural Strain (ANS) methods with phase field of fracture is exploited. In order to achieve realistic prediction, the crack driving force is computed using positive/negative split of the stress field. Moreover, the difference between the driving forces are pinpointed. Furthermore, based on thermodynamic considerations, the free energy function is modified to introduce the fatigue effect via a degradation of the material fracture toughness. This approach retrieves the SN curves and the crack growth curve as expected. The predictive capability of the model is evaluated through benchmark examples that include a plate with a notch, a curved shell, mode II shear, and three-point bending for homogeneous materials, as well as a dogbone specimen for homogenized fiber-reinforced composites. Additionally, comparative analysis is performed with previous results for the plate with notch and mode II shear tests, while the dogbone specimen is compared with experimental data to further validate the accuracy of the present model.

1. Introduction

Fracture induced by fatigue loading is considered one of the most frequent damages accounting for up to 90% of all material failures [1]. Its complex nature and inability to predict beforehand make it an extremely dangerous failure modes. In classical material science, fatigue is attributed to material weakening due to small repeated loading. Micro-cracks develop energetically as a consequence of sub- or micro-structural changes in the material. These micro-cracks further depend on the material's microstructure, ruled by a stochastic process, and eventually coalesce and leads to a macro-crack, where its size is sufficiently large enough to overcome the microstructure's energy barrier to nucleate, eventually leading to failure.

The early studies regarding fatigue failure are dominated by empirical relations such as Wöhler curves [2], Paris law [3,4], Coffin [5], and Manson [6] ideas, based on extensive experimental data fitting methods, see also [7] for a systematic review. Wöhler noticed the number of cycles (N) at failure for an applied stress amplitude σ_a follows a power-law equation:

$$\sigma_a = AN^{\beta},$$

for some constants A and β that depend on the material and many other environmental factors. This approach beholds some important observations, such as the presence of a threshold amplitude below which the material is unlikely to fail. Based in the number of cycles to failure N, fatigue can be broadly classified as (i) Ultra-low/oligo-cycle fatigue (ULC), (ii) Low cycle fatigue (LC), and (iii) High cycle fatigue (HC) [8].

Following Wöhler, Palmgren [9] and Miner [10] introduced the idea of cumulative damage. For k different stress amplitudes occurring in a loading history, the damage contribution, independent of the order of applied loads, gives $\eta_i = \frac{1}{N\sigma_a^i}$, for $i = 1, k$. Later, Paris [3] showed from experiments that in a single cycle with crack length $'a'$, the rate

* Corresponding author at: .
E-mail address: pavan.kumar@ilsb.tuwien.ac.at (P.K. Asur Vijaya Kumar).

https://doi.org/10.1016/j.tafmec.2023.104029
Received 30 April 2023; Received in revised form 24 July 2023; Accepted 24 July 2023
Available online 3 August 2023

of change of crack length $\frac{\mathrm{d}a}{\mathrm{d}N}$ is a power-law function to the stress intensity factor range ΔK, as

$$\frac{\mathrm{d}a}{\mathrm{d}N} = C\Delta K^m,$$

for some constants C and m that depend on the material.

The aforementioned fatigue life models, one based on overall damage accumulation and another based on the propagation of a crack, have been found experimentally and the related scaling laws have been largely confirmed by dimensional analysis considerations in [7].

Besides the above fatigue life models, phenomenological and progressive damage models were also proposed in literature. On the basis of experimentally determined damage evolution equations, phenomenological models [11–14] predict macroscopic material deterioration (stiffness and strength) taking into consideration stress redistributions during the structural fatigue analysis. Progressive damage models [15–21], on the other hand, take into account the physical evolution of damage and relate it to the stiffness and the strength properties. Such models category possesses the capacity of accounting for the effects of loading sequence and stress redistribution.

In recent years, the variational approach to fracture, known as the phase-field approach, has been extended to include fatigue behavior. In this approach, fatigue is considered as a degradation of the fracture energy, achieved by introducing scalar parameters dependent on factors such as stress, bulk energy, $\mathcal{G}_C$, and the internal length scale of nonlocal damage l_c, among others. Boldrini et al. [22] presented a thermo-mechanical phase-field fatigue model by introducing an additional scalar parameter. Schreiber et al. [23] proposed an additional energy contribution to the total energy. A more intuitive approach to fatigue was proposed by Carrara et al. [24–28], where the stiffness and fracture energy were degraded as a function of cumulative stored potential. As a natural consequence, these models accurately recover Paris-law and S-N curves, making them self-consistent. Seiler et al. [27] applied a local strain approach empirically to incorporate plasticity using Neuber's rule. Schreiber et al. [23] employed Miner's rule to govern fatigue evolution. Following [29] work, many others have proposed the accumulation of strain energy either via strain energy [23,24,26,28,30–33], or elastoplastic energy density [28,33]. Regarding the high cycle fatigue, Seles et al. [26] proposed a cycle jumping technique to efficiently capture high-cycle fatigue. Additionally, a robust quasi-Newton method for fatigue is proposed in [34], and high-cycle fatigue is suggested in [35,36].

In this work, a phase-field fracture model is proposed for the analysis of structures subjected to fatigue/cyclic loading with full integration solid-shells capable of handling both thin and thick shells. The shell body is first parameterized with a top and a bottom surface of the body as in [37–41]. Due to the intrinsic nature of finite elements with lower order kinematic interpolation, shells undergo numerical locking. To obtain a locking free shell with full integration, the proposed model is equipped with the Enhanced Assumed Strain (EAS) [42–46] to alleviate the volumetric and Poisson's thickness locking effects, whereas the Assumed Natural Strain (ANS) [47,48] is used to treat trapezoidal and transverse shear locking. Shell structures damage, have been used in numerous literature whose description is provided via XFEM [49–52], isoparametric analysis [53–55], gradient enhanced damage methods [56–59]. Recently thermo-mechanical analysis of thin walled structure with full integration that includes EAS and ANS method has been discussed in [60–63]. In the phase field literature, three different kind of split of strain energy is proposed: (i) volumetric-deviatoric split [64,65], where the crack is driven by volumetric expansion and deviatoric strains, (ii) spectral split [66–68] where strain/stress decomposed into its principal components, (iii) directional split based on stress decomposition [69].

Solid-shell elements are naturally solved in curvilinear co-ordinates since they allow more natural representation of the curved geometry of the shell. In curvilinear coordinates, the forces acting on a material point are not necessarily co-linear with the coordinate axis and therefore cannot be described by a single scalar value at that point. The Cauchy stress tensor allows to describe the forces at a material point in all directions, making it a more general and useful concept. This is particularly important in the analysis of shells with complex geometries, where the use of curvilinear coordinates is common. Furthermore, a crack driving force is herein computed via spectral decomposition of the Cauchy stresses. As a consequence of this driving force, the fracture involving mixed modes can be captured in the solid shell (see 5.3) otherwise leading to the ad hoc criteria. In Section 5.3, we elucidate the difference between the conventional driving force and the driving force based on the split, where the dominance of mode II is highlighted. Our findings suggest that the regular driving force leads to the formation of Mode I crack, consistent with the outcomes reported in [69]. Furthermore, our investigation in Section 5.4 demonstrates that the combination of the driving force based on the split with thick shells can effectively capture structures that require an ad hoc criteria for thin shells. In addition, our results indicate that the proposed solid shell model can replicate the behavior of thick shells, similar to that of the conventional solids (see Section 5.4). Consequently, the proposed solid shell model can serve as a link between solid and shell structures. A link for the codes used in this article is provided.

The model can be readily extended to analyze homogenized fiber-reinforced composites (FRCs). Several authors have proposed fracture theories for FRCs, which can be found in [70,71] and others cited therein. Additionally, the analysis of composites within the context of solid shells has been addressed in [40]. The extended model is compared with experimental results in [72] for low cycle fatigue to verify its accuracy.

For a comprehensive outlook, the article is organized as follows: Section 2.1 outlines the theoretical aspects of the solid-shell finite element formulation. Section 3 presents the variational basis and the thermodynamic consistency of the proposed fatigue model with particular emphasis on the computation of the crack driving force. Section 4 presents the finite element treatment and implementation of the proposed formulation. Section 5 examines the application of proposed model in relation to several benchmark examples. The choice of examples to demonstrate the capabilities of the model are pinpointed. In particular, Section 5.1 is presented for comparison with the previous results presented in 2D plane strain condition in [24]. The extension of the model to analyze homogenized fiber-reinforced composites is presented in 18. The accuracy of the extended model is verified by comparing its results with experimental data [72] for low cycle fatigue, and the model demonstrates satisfactory agreement with the experimental results. Section 5.2 is presented to show the model capability to handle lockings. Pure Mode II shear benchmark test is proposed in Section 5.3 to examine the Cauchy-based stress split in both monotonic and cyclic loading, where the difference between Cauchy based split and regular driving force is pinpointed. Section 5.4 exemplifies three-point bending as a means of extending the model's capabilities to thick structures while avoiding locking in thin shells. Finally, the main conclusions are drawn in Section 6.

2. Modeling framework

2.1. Kinematics

Let $\mathcal{B}_0 \subset \mathbb{R}^3$ be a body in the reference configuration of an three-dimensional Euclidean space with its delimiting boundary $\partial\mathcal{B}_0 \subset \mathbb{R}^2$. The external boundary can be split into $\partial\mathcal{B}_{0,u}$, and $\partial\mathcal{B}_{0,\bar{t}}$ to accommodate Dirichlet and Neumann boundary conditions respectively such that $\partial\mathcal{B}_{0,u} \cap \partial\mathcal{B}_{0,\bar{t}} = \emptyset$ and $\partial\mathcal{B}_0 = \overline{\partial\mathcal{B}_{0,u} \cup \partial\mathcal{B}_{0,\bar{t}}}$.

For every $\mathbf{X} \in \mathcal{B}_0$, define a vector-valued displacement $\mathbf{u} = \mathbf{u}(\mathbf{X}, t) : \mathcal{B}_0 \times [0,t] \rightarrow \mathbb{R}^3$, a smooth scalar-valued damage function $\mathfrak{d}(\mathbf{X}, t) : \mathcal{B}_0 \times [0,t] \rightarrow [0,1]$, for some time interval $t \in [0,T]$. The body $\mathcal{B}_0$ under external forces undergoes motion $\boldsymbol{\varphi}(\mathbf{X}, t) \in \mathcal{V}$ such that $\boldsymbol{\varphi}$ maps

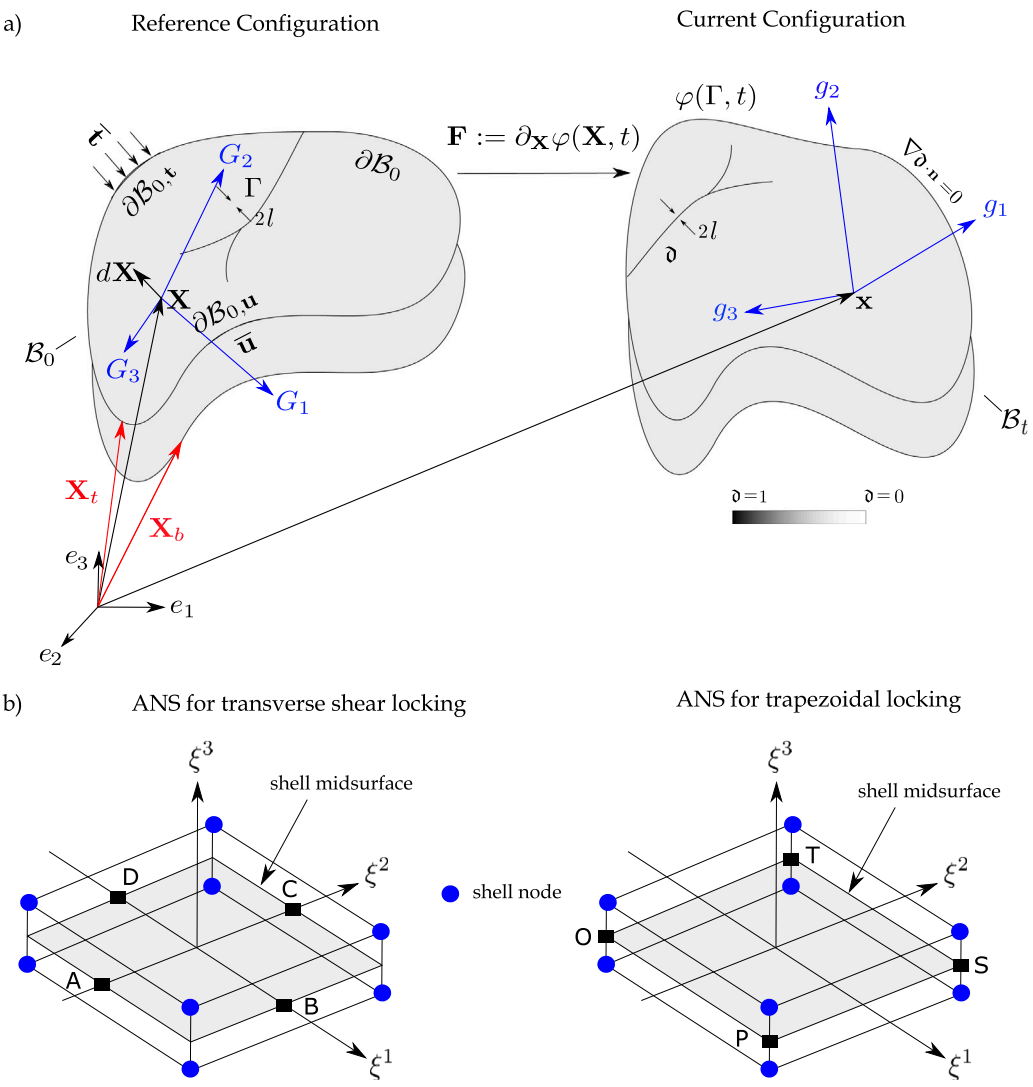

Fig. 1. (a) Finite deformation of a body: reference and current configurations. Deformation mapping $\boldsymbol{\varphi}(\mathbf{X},t)$, that transforms at time t the reference configuration $\mathcal{B}_0$ onto the current configuration $\mathcal{B}_t$, and (b) collocation points for the ANS interpolation to remedy the transverse shear and trapezoidal locking pathologies.

every $\mathbf{X} \in \mathcal{B}_0$ onto a current configuration $\mathbf{x} \in \mathcal{B}_t$ for each t. i.e $\mathbf{x} = \boldsymbol{\varphi}(\mathbf{X},t) = \mathbf{X} + \mathbf{u}(\mathbf{X},t)$, see Fig. 1a.

Here $\mathcal{V}$ is a space of admissible functions (map) defined as

$$\mathcal{V} := \left\{\varphi : \mathcal{B}_0 \times [0,t] \to \mathbb{R}^{n_{dim}} | \varphi \in W^{1,p}(\mathcal{B}_0) \quad \text{and} \quad \varphi = \bar{\varphi} \right.$$
$$\left. \text{on} \quad \partial\mathbb{R}_u \quad \text{for} \quad p \geq 2\right\},$$

where $W^{1,p}$ is the Lipschitz regular Sobolev space.

The displacement derived non-linear deformation gradient $\mathbf{F}^u$ maps the unit line elements $\mathrm{d}\mathbf{X}$ in the reference configuration onto current line element $\mathrm{d}\mathbf{x} = \mathbf{F}^u\mathrm{d}\mathbf{X}$, whose particular expression in the curvilinear setting can be written as

$$\mathbf{F}^u := \partial_{\mathbf{X}}\boldsymbol{\varphi}(\mathbf{X},t) = \frac{\partial \mathbf{x}}{\partial \mathbf{X}} \in \mathbb{R}^{3\times3},$$

where

$$\mathbf{G_i}(\xi) := \frac{\partial \mathbf{X}(\xi)}{\partial \xi^i}, \quad \mathbf{g_i}(\xi) := \frac{\partial \mathbf{x}(\xi)}{\partial \xi^i}, \qquad i = \{1,2,3\},$$

are the covariant basis in reference and current configuration, respectively. The jacobian of the transformation $\mathbf{F}^u$ satisfies $J^u := \det[\mathbf{F}^u] > 0$. Moreover, with the usual notation, a metric tensor $\chi \in \mathbb{R}^{3\times3}$ can be written in their covariant χ_{ij} and contravariant χ^{ij} components as $\chi = \chi_{ij}\chi^i \otimes \chi^j = \chi^{ij}\chi_i \otimes \chi_j$. Here, (χ_i, χ^i) are covariant and contravariant basis vector such that χ_i and χ^i are perpendicular to each other. i.e $\chi_i\chi^j = \delta_i^j$. Furthermore, as a consequence of the curvilinear co-ordinates, the Green–Lagrangian strain tensor $\mathbf{E}^u$ and second Piola–Kirchhoff stress tensor $\mathbf{S}$ (PK2) is derived via Cauchy–Green deformation and elasticity tensor respectively, whose particular expressions in the reference configuration takes the form

$$\mathbf{E}^u := \frac{1}{2}\left[g_{ij} - G_{ij}\right]\mathbf{G}^i \otimes \mathbf{G}^j; \qquad \mathbf{S} = \mathbb{C} : \mathbf{E}^u = S^{ij}\mathbf{G}_i \otimes \mathbf{G}_j, \tag{1}$$

where g_{ij} and G_{ij} are the covariant metric tensor components in the current and reference configuration, respectively. Complying with the standard solid-shell approach, the position vector in the reference $\mathbf{X}$ and current configuration $\mathbf{x}$ are expressed in the parametric space $\mathcal{A} := \{\boldsymbol{\xi} = (\xi^1,\xi^2,\xi^3) \in \mathbb{R}^3 \mid -1 \leq \xi^i \leq +1; i = 1,2,3\}$ of natural co-ordinates as a linear combination of in-plane (ξ^1,ξ^2) points on the top/bottom surface $\mathbf{X}_t/\mathbf{X}_b \in \mathbb{R}^2$. i.e

$$\mathbf{X}(\boldsymbol{\xi}) = \frac{1}{2}\left(1+\xi^3\right)\mathbf{X}_t(\xi^1,\xi^2) + \frac{1}{2}\left(1-\xi^3\right)\mathbf{X}_b(\xi^1,\xi^2),$$

and

$$\mathbf{x}(\boldsymbol{\xi}) = \frac{1}{2}\left(1+\xi^3\right)\mathbf{x}_t(\xi^1,\xi^2) + \frac{1}{2}\left(1-\xi^3\right)\mathbf{x}_b(\xi^1,\xi^2).$$

Consequently, the phase-field variable $\mathfrak{d}$ in $\mathcal{A}$ is also estimated as a linear combination of top ($\mathfrak{d}_t$) and bottom ($\mathfrak{d}_b$) value as

$$\mathfrak{d}(\boldsymbol{\xi}) = \frac{1}{2}\left(1+\xi^3\right)\mathfrak{d}_t(\xi^1,\xi^2) + \frac{1}{2}\left(1-\xi^3\right)\mathfrak{d}_b(\xi^1,\xi^2),$$

with $\mathfrak{d}_t : \mathcal{B}_0 \supset \mathbf{X}_t \times [0,T] \to [0,1]$ and $\mathfrak{d}_b : \mathcal{B}_0 \supset \mathbf{X}_b \times [0,T] \to [0,1]$.

Regarding the enrichment based on Enhanced Assumed Strain (EAS), the total Green–Lagrangian strain ($\mathbf{E}$) is additively decomposed into displacement derived Green–Lagrangian strain $\mathbf{E}^u$ and incompatible strain $\tilde{\mathbf{E}}$ stemming from EAS. i.e

$$\mathbf{E} := \mathbf{E}^u + \tilde{\mathbf{E}}. \tag{2}$$

As a consequence of the decomposition in Eq. (2), displacement derived deformation gradient $\mathbf{F}^u$ is modified to accommodate incompatible deformation gradient $\tilde{\mathbf{F}}$ as $\mathbf{F} = \mathbf{F}^u + \tilde{\mathbf{F}}$. The modified Jacobian then takes the form $J := \det[\mathbf{F}] > 0$.

2.2. Extension to layered composite materials

Concerning the constitutive formulation for unidirectional laminated composites, the use of the so-called equivalent single layer (ESL) approach is exploited. ESL models are generally applied to thin and moderately-thin composite specimens with similar stiffness properties between the compositing layers. This simplified method for the macroscopic analysis of UD composite laminates consists of replacing the heterogeneous laminate by a weighted average of the physical properties of each ply across the thickness. In line with the procedure described in [40], the constitutive relationship between the second Piola–Kirchhoff stress tensor $\mathbf{S} = S^{ij}\mathbf{G}_i \otimes \mathbf{G}_j$ and the Green–Lagrange strain tensor $\mathbf{E} = E_{ij}\mathbf{G}^i \otimes \mathbf{G}^j$ is given by

$$\mathbf{S} = \mathbb{C} : \mathbf{E}, \tag{3}$$

The previous relationship is defined in the global setting $\{\mathbf{G}_1, \mathbf{G}_2, \mathbf{G}_3\}$ in the reference configuration and can be transformed into the current configuration by standard push-forward operations. Moreover, $\mathbf{S} = \mathbb{C} : \mathbf{E}$ requires the transformation from local material setting at lamina level (usually complying with orthotropic material law), denoted by $\mathbb{C}_L$ to the global setting is required. This can be carried out by the following operations using the rotation matrices $\mathbf{Q}$ from the local material setting $\{\mathbf{G}_1^*, \mathbf{G}_2^*, \mathbf{G}_3^*\}$ to the global setting $\{\mathbf{G}_1, \mathbf{G}_2, \mathbf{G}_3\}$ for the lamina L:

$$\mathbb{C}_L^{ijkl} = Q_{mi}Q_{nj}\mathbb{C}_L^{mnop*}Q_{ok}Q_{pl} \quad i,\ldots,p = 1,2,3 \quad \text{with}$$
$$\mathbf{Q} = Q_{ij} = \mathbf{G}_i^*\mathbf{G}_j, \quad \mathbf{G}_i^* = \mathbf{Q}\mathbf{G}_j \tag{4}$$

The total constitutive tensor for laminates is constructed by taking into account the weighted-averaged location and lamina thickness using:

$$\mathbb{C}(\xi^3)\begin{cases} \mathbb{C}_{N_L} & \bar{\xi}^3_{N_L} \le \xi^3 \le \bar{\xi}^3_{N_L+1} = +1 \\ \mathbb{C}_{N_L-1} & \bar{\xi}^3_{N_L-1} \le \xi^3 \le \bar{\xi}^3_{N_L} \\ \ldots. & \ldots.. \\ \mathbb{C}_2 & \bar{\xi}^3_2 \le \xi^3 \le \bar{\xi}^3_3 \\ \mathbb{C}_1 & -1 = \bar{\xi}^3_1 \le \xi^3 \le \bar{\xi}^3_2 \end{cases}, \tag{5}$$

where the coordinate $\xi^3 \in [-1,+1]$, once it is scaled by the total laminate thickness H; $H = \sum_{L=1}^{N_L} H_L$ with N_L standing for the number of layers and H_L rendering the lamina thickness; and where shell coordinate midsurface of each layer i, ξ_i^3, can be computed as:

$$\xi_i^3 = -1 + \frac{H_i}{H} + \frac{2}{H}\sum_{j=1}^{i-1} H_j \quad i=1,\ldots,N_L \tag{6}$$

Finally, with respect to the consideration of a fracture toughness for the multi-directional (MD) laminate, we recall the procedure recently proposed by [73] in which a modification of the anisotropic PF formulations was developed in order to obtain G_C using singular lamina properties and lay-up disposals, in conjunction with accounting for the variation of the fracture toughness in different laminate directions. We omit specific details for this approximation for the sake of brevity.

3. Variational basis and finite element formulation

Based on the energy approach, a crack occurs as a macroscopic manifestation of debonding at a microscopic level. This failure process can be accurately presented as the competition between bulk energy (due to applied load) and crack surface energy (due to creation of new surfaces) at each point. Within this context, the total energy $\Pi(\mathbf{u}, \Gamma_t)$ with the crack set Γ_t at any given time $t \in [0,T]$ can be written as minimization problem in set $S = \{\dot{\mathfrak{d}} \ge 0 \text{ for all } \mathbf{X} \in B_0|\Gamma_t,\ \Gamma_{t+1} \supset \Gamma_t\}$ as

$$(\mathbf{u}^*, \Gamma_t) := \arg\min_S \Pi(\mathbf{u}, \Gamma_t)$$
$$= \arg\min_S \left\{ \int_{\mathcal{B}_0/\Gamma_t} \Psi(\mathbf{u}, \Gamma)\mathrm{d}\Omega + \int_{\Gamma_t} G_C \mathrm{d}\Gamma + \Pi_{ext} \right\}. \tag{7}$$

Here, $\Psi(\mathbf{u}, \Gamma)$ is the energy density, Π_{ext} is the external potential, and G_c is the fracture toughness. Based on the elliptical regularization of the free-discontinuity functions [74], the above functional can be approximated using diffusive crack approach by introducing a smeared scalar field $\mathfrak{d} \in [0,1]$ as

$$\Pi(\mathbf{u}, \mathfrak{d}) = \int_{\mathcal{B}_0} g(\mathfrak{d})\Psi_0(\mathbf{u})\mathrm{d}\Omega + \int_{\mathcal{B}_0} \frac{G_c}{4c_w}\left[\frac{\alpha(\mathfrak{d})}{l} + l\,|\nabla\mathfrak{d}|^2\right] \mathrm{d}\Omega + \Pi_{\text{ext}}. \tag{8}$$

for some external force Π_{ext}. Here

1. function $g(\mathfrak{d})$ is degradation function characterized as $g(\mathfrak{d}) : [0,1] \to [1,0]$, and it is a monotonically decreasing function that satisfies $g(0) = 1$, $g(1) = 0$, and $\frac{\mathrm{d}g}{\mathrm{d}\mathfrak{d}} < 0$.
2. function $\alpha(\mathfrak{d})$ is characterized as a geometric crack function such that $\alpha(0) = 0$, $\alpha(1) = 1$, and $c_w := \int_0^s \sqrt{\alpha(s)}\mathrm{d}s$ is the normalization parameter.
3. $\Psi_0(\mathbf{u})$ represents the elastic energy density of the unbroken solid.

Taking into consideration the solid-shell formulation using multi-field Hu–Washizu variational principle and fatigue effects, Eq. (8) is modified as follows

$$\Pi(\mathbf{u}, \tilde{\mathbf{E}}, \mathfrak{d}) = \int_{\mathcal{B}_0} g(\mathfrak{d})\Psi_0(\mathbf{u}, \tilde{\mathbf{E}})\mathrm{d}\Omega - \int_{\mathcal{B}_0} \mathbf{S} : \tilde{\mathbf{E}}\ \mathrm{d}\Omega$$
$$+ \int_{\mathcal{B}_0} f(\bar{\alpha}(t))\frac{G_c}{4c_w}\left[\frac{\alpha(\mathfrak{d})}{l} + l\,|\nabla\mathfrak{d}|^2\right] \mathrm{d}\Omega + \Pi_{\text{ext}}. \tag{9}$$

where $\Psi_0(\mathbf{u}, \tilde{\mathbf{E}})$ is the intact elastic energy density function which involves incompatible strains, function $f(\bar{\alpha})$ represents the fatigue degradation, and $\bar{\alpha}(t)$ is a function that defines a suitable cumulative history variable (to be defined).

The thermodynamic consistency of the total energy functional Eq. (9) can be ensured by considering rate dissipation density potential

$$\dot{\mathcal{D}} = \left[\mathbf{S} - \partial_{\mathbf{E}}\Pi\right] : \dot{\mathbf{E}} - \partial_{\mathfrak{d}}\Pi : \dot{\mathfrak{d}} \ge 0. \tag{10}$$

Expanding the second term $\partial_{\mathfrak{d}}\Pi : \dot{\mathfrak{d}}$ leads to

$$\partial_{\mathfrak{d}}\Pi : \dot{\mathfrak{d}} = \frac{\mathrm{d}g}{\mathrm{d}\mathfrak{d}}\Psi_0(\mathbf{u}, \tilde{\mathbf{E}}) : \dot{\mathfrak{d}} + f(\bar{\alpha}(t))\frac{G_c}{4c_w}\left[\frac{\mathrm{d}\alpha(\mathfrak{d})}{\mathrm{d}\mathfrak{d}}\frac{\dot{\mathfrak{d}}}{l} + 2l\nabla\mathfrak{d}\cdot\nabla\dot{\mathfrak{d}}\right].$$

Integrating by parts the expression gives

$$-\partial_{\mathfrak{d}}\Pi : \dot{\mathfrak{d}} = \frac{\mathrm{d}g}{\mathrm{d}\mathfrak{d}}\Psi_0(\mathbf{u}, \tilde{\mathbf{E}}) : \dot{\mathfrak{d}} - \frac{G_c}{4c_w}l\left[\left(\Delta\mathfrak{d} - \frac{\mathrm{d}\alpha}{\mathrm{d}\mathfrak{d}}\frac{1}{2l^2}\right) f(\bar{\alpha}) + \nabla f(\bar{\alpha})\cdot\nabla\mathfrak{d}\right]\dot{\mathfrak{d}}.$$

In order for Eq. (10) to hold, $\frac{\mathrm{d}g}{\mathrm{d}\mathfrak{d}}\Psi_0(\mathbf{u},\tilde{\mathbf{E}}) \geq 0$, $\dot{\mathfrak{d}} \geq 0$, $f_d(\mathfrak{d}, \Delta\mathfrak{d}, f(\bar{\alpha})) \geq 0$ leading to

$$f_d(\mathfrak{d}, \Delta\mathfrak{d}, f(\bar{\alpha})) = \frac{G_c}{4c_w} l \left[\left(\Delta\mathfrak{d} - \frac{\mathrm{d}\alpha}{\mathrm{d}\mathfrak{d}} \frac{1}{2l^2} \right) f(\bar{\alpha}) + \nabla f(\bar{\alpha}) \cdot \nabla\mathfrak{d} \right] \geq 0,$$

$$\frac{\mathrm{d}g}{\mathrm{d}\mathfrak{d}}\Psi_0(\mathbf{u},\tilde{\mathbf{E}}) \geq 0; \qquad \dot{\mathfrak{d}} \geq 0; \qquad f_d(\mathfrak{d}, \Delta\mathfrak{d}, f(\bar{\alpha}))\dot{\mathfrak{d}} = 0; \qquad f(\bar{\alpha}) \cdot \nabla\mathfrak{d} \cdot \boldsymbol{n} \geq 0. \tag{11}$$

Notice that, due to choice of $g(\mathfrak{d})$, the function $\frac{\mathrm{d}g}{\mathrm{d}\mathfrak{d}}\Psi_0(\mathbf{u})$ naturally holds true, leading to the first order stability conditions or KKT conditions

$$\dot{\mathfrak{d}} \geq 0; \qquad f_d(\mathfrak{d}, \Delta\mathfrak{d}, f(\bar{\alpha})) \geq 0; \qquad f_d(\mathfrak{d}, \Delta\mathfrak{d}, f(\bar{\alpha}))\dot{\mathfrak{d}} = 0. \tag{12}$$

Notice from Eq. (9) that fatigue degradation function $f(\bar{\alpha})$ should be locally integrable, and from Eq. (12) to be true, $0 \leq f(\bar{\alpha}) \leq 1$. Since $f(\bar{\alpha})$ degrades the crack energy (to be specific fracture toughness G_c), $f(\bar{\alpha})$ should be also monotonically decreasing function. i.e $f'(\bar{\alpha}) \leq 0$ for $f(\bar{\alpha}) \in [0, 1]$.

3.1. Choice of functions

3.1.1. Geometric crack function

The geometric crack function $\alpha(\mathfrak{d}) = \mathfrak{d}^2$ is herein considered as in [66]. With $\alpha(\mathfrak{d}) = \mathfrak{d}^2$, the phase-field problem renders linear (within a staggered scheme) and this is making the computation easier and cheaper. Moreover, $\mathfrak{d} \in [0, 1]$ can be ensured easily without any ad-hoc treatments.

3.1.2. Stored energy function

The stored energy function describes the equilibrium state that defines the behavior of a solid in the unbroken state (i.e $\mathfrak{d} = 0$). A modification or rather choice of $\Psi_0(\mathbf{u})$ in Eq. (9) presents different models such as brittle, ductile, plastic, thermo-elastic, thermo-plastic, viscous, etc. In this work, we only use

1. Isotropic elastic body whose stored energy density is defined as

$$\Psi_0(\mathbf{E}) = \frac{1}{2}\mathbf{E} : \mathbb{C} : \mathbf{E} = \frac{1}{2}\lambda \mathbf{tr}^2(\mathbf{E}) + \mu\mathbf{E} : \mathbf{E}. \tag{13}$$

Here, $\mathbb{C}$ defines the linear elasticity tensor whose particular expression in the curvilinear co-ordinates takes

$$\mathbb{C} = \partial_{\mathbf{EE}}\Psi_0 = \left[\lambda G^{ij}G^{kl} + \mu\left(G^{ik}G^{jl} + G^{il}G^{jk}\right)\right] \mathbf{G}_i \otimes \mathbf{G}_j \otimes \mathbf{G}_k \otimes \mathbf{G}_l, \tag{14}$$

where λ and μ denotes the Lame's constant.

2. Tension/Compression split, where the stored energy density is split into tension/compression to prevent cracking under compressive loads as

$$\Psi(\mathbf{E}) = g(\mathfrak{d})\Psi_0(\mathbf{E}) = g(\mathfrak{d})\Psi_0^+(\mathbf{E}) + \Psi_0^-(\mathbf{E}). \tag{15}$$

Notice that, as a natural consequence of the formulation, the stresses are the second Piola–Kirchhoff tensor $\mathbf{S}$ (PK2) whose particular expression in the curvilinear setting takes the form

$$\mathbf{S} = S^{ij}\mathbf{G}_i \otimes \mathbf{G}_j, \tag{16}$$

where S^{ij} identifies its contravariant components. In order to compute the stress split, first, the components of $\mathbf{S}$ should to be transformed to Cartesian coordinate using the covariant basis vector in the reference configuration.
The components of Cauchy stress σ in the Cartesian system under small strain assumptions can then be computed from

$$\boldsymbol{\sigma} = J^{-1}\mathbf{F} \cdot \mathbf{S} \cdot \mathbf{F}^T. \tag{17}$$

Based on this, the total energy density takes the form

$$\Psi_0(\boldsymbol{\varepsilon})^+ = \frac{1}{2E}\left[(1+\mu)(\sigma_1^2 + \sigma_2^2 + \sigma_3^2) - \mu(\mathrm{tr}(\boldsymbol{\sigma}^+))^2\right], \tag{18}$$

where $\sigma_1, \sigma_2, \sigma_3$ are principal stresses and $\boldsymbol{\sigma}^+ = \frac{1}{2}(|\boldsymbol{\sigma}| + \boldsymbol{\sigma})$.

3.1.3. Energetic degradation function

Energetic degradation function $g(\mathfrak{d})$ plays a major role of linking elastic energy and crack phase-field $\mathfrak{d}$ by degrading the elastic energy Ψ_0. We adopt $g(\mathfrak{d}) = (1-\mathfrak{d})^2$ as originally proposed by [75]. Since $\mathfrak{d}$ is bounded, naturally $g(\mathfrak{d})$ is bounded with $g(1) = 0$, and $g(0) = 1$ representing fully damaged and intact material respectively.

3.1.4. Cumulative history variable

The term $\bar{\alpha}(t)$ in Eq. (9) describes the cumulative history effects due to fatigue. We adopt the function proposed by Carrara et al. [24] where

1. $\bar{\alpha}(t)$ is independent of the mean load defined as

$$\bar{\alpha}(\mathbf{x}, t) = \int_0^t H(\alpha\dot{\alpha})|\dot{\alpha}|d\tau. \tag{19}$$

2. For a normalization parameter α_N, mean load dependent cumulative history variable can be defined as

$$\bar{\alpha}(\mathbf{x}, t) = \frac{1}{\alpha_N}\int_0^t H(\alpha\dot{\alpha})\alpha\dot{\alpha}d\tau, \tag{20}$$

for $\alpha = \Psi(\mathbf{E}, \mathfrak{d})$ is the total degraded strain energy which ensures that the model is not affected by crack tip singularity. See [24, 76] for more details. In the case where tension/compression spilled is used for the elastic energy, then, $\alpha = \Psi^+(\mathbf{E}, \mathfrak{d})$ is used to distinguish between active tensile/compressive part. Here $H(\alpha\dot{\alpha})$ is Heavyside function defined as

$$H(\alpha\dot{\alpha}) = \begin{cases} 1 & \alpha\dot{\alpha} \geq 0 \quad \text{(Loading)} \\ 0 & \text{otherwise (Unloading).} \end{cases} \tag{21}$$

3.1.5. Fatigue degradation function

The function $f(\bar{\alpha})$ describes the degradation of the material property due to repeated loading. The functions can be mainly categorized into asymptotic degradation (i.e as $\bar{\alpha}(t) \to \infty, f(\bar{\alpha}) \to 0$) and symptotic degradation (i.e for $\bar{\alpha}(t) > \alpha_\infty, f(\bar{\alpha}) = 0$) for some cut-off function α_∞.
The generalized asymptotic degradation function is defined as

$$f(\bar{\alpha}) = \begin{cases} 1 & \text{if } \bar{\alpha}(t) \leq \alpha_T \\ \left(\frac{2\alpha_T}{\bar{\alpha}(t) + \alpha_T}\right)^a & \text{if } \bar{\alpha}(t) \geq \alpha_T \end{cases} \tag{22}$$

for some threshold α_T before which the fatigue degradation is not triggered. Whereas the symptotic degradation function is defined as

$$f(\bar{\alpha}) = \begin{cases} 1 & \text{if } \bar{\alpha}(t) \leq \alpha_T \\ \left[1 - k\, log\frac{\bar{\alpha}(t)}{\alpha_T}\right]^2 & \text{if } \alpha_T \leq \bar{\alpha}(t) \leq \alpha_T 10^{\frac{1}{k}} \\ 0 & \text{if } \bar{\alpha}(t) \geq \alpha_T 10^{\frac{1}{k}} \end{cases} \tag{23}$$

Here, a and k are the material constant that can be used to control the fatigue degradation.

4. Finite element implementation

For any admissible test functions $\delta\mathbf{u} \in \mathfrak{B}^u$, $\delta\tilde{\mathbf{E}} \in \mathfrak{B}^{\tilde{E}}$, $\delta\mathfrak{d} \in \mathfrak{B}^{\mathfrak{d}}$, with functional space defined as

$$\mathfrak{B}^u = \{\delta\mathbf{u} \in \mathbf{H}^1(\mathcal{B}_0),\ \delta\mathbf{u} = 0 \text{ on } \partial\mathcal{B}_{0,\mathbf{u}}\}, \tag{24a}$$

$$\mathfrak{B}^{\tilde{E}} = \{\delta\tilde{E} \in \mathbf{L}^2(\mathcal{B}_0)\}, \tag{24b}$$

$$\mathfrak{B}^{\mathfrak{d}} = \{\delta\mathfrak{d} \in H^1(\Omega) \,|\, \delta\mathfrak{d} \geq 0 \,\forall\, \mathbf{X} \in \mathcal{B}_0\}, \tag{24c}$$

the set $(\mathbf{u}, \tilde{\mathbf{E}}, \mathfrak{d})$ is obtained by taking first variation of Eq. (9) leading to the following multi-field problem

$$\mathcal{R}^{u}(\mathbf{u}, \tilde{\mathbf{E}}, \mathfrak{d}, \delta\mathbf{u}) = \int_{\mathcal{B}_0} g(\mathfrak{d}) \left[\mathbf{S} : \delta\mathbf{E}^{u}\right] \, \mathrm{d}\Omega - \mathcal{R}^{u}_{\text{ext}} = 0 \tag{25a}$$

$$\mathcal{R}^{\tilde{E}}(\mathbf{u}, \tilde{\mathbf{E}}, \mathfrak{d}, \delta\tilde{\mathbf{E}}) = \int_{\mathcal{B}_0} \left[\mathbf{S} : \delta\tilde{\mathbf{E}}\right] \, \mathrm{d}\Omega = \mathcal{R}^{\tilde{E}}_{\text{int}} = 0, \tag{25b}$$

$$\begin{aligned}\mathcal{R}^{\mathfrak{d}}(\mathbf{u}, \tilde{\mathbf{E}}, \mathfrak{d}, \delta\mathfrak{d}) = &\int_{\mathcal{B}_0} f(\bar{\alpha}(t)) G_C \left[\frac{\mathfrak{d}}{l}\delta\mathfrak{d} + l\nabla\mathfrak{d}\cdot\nabla\delta\mathfrak{d}\right] \, \mathrm{d}\Omega \\ &- \int_{\mathcal{B}_0} 2(1-\mathfrak{d})\Psi(\mathbf{u}, \tilde{\mathbf{E}})\delta\mathfrak{d} \, \mathrm{d}\Omega = 0,\end{aligned} \tag{25c}$$

The functional space $\mathcal{B}_0$ is discretized into n_e non-overlapping elements such that partition of unity holds. i.e., $\mathcal{B}_0 \approx \bigcup_{e=1}^{n_e} \mathcal{B}_0^{(e)}$ for n_e.

The position vectors in reference and current configuration are interpolated using standard tri-linear shape function $\mathbf{N}(\boldsymbol{\xi})$ in natural co-ordinates $\boldsymbol{\xi} = \{\xi^1, \xi^2, \xi^3\}$ as

$$\mathbf{X} \approx \sum_{I=1}^{8} N^I(\boldsymbol{\xi})\mathbf{X}_I = \mathbf{N}(\boldsymbol{\xi})\widetilde{\mathbf{X}} \quad \text{and } \mathbf{x} \approx \sum_{I=1}^{8} N^I(\boldsymbol{\xi})\mathbf{x}_I = \mathbf{N}(\boldsymbol{\xi})\widetilde{\mathbf{x}},$$

for global vectors $\widetilde{\mathbf{X}}$ and $\widetilde{\mathbf{x}}$ in reference and current configuration respectively. Similarly, the unknown fields $(\mathbf{u}, \tilde{\mathbf{E}}, \mathfrak{d})$ and their variations $(\delta\mathbf{u}, \delta\tilde{\mathbf{E}}, \delta\mathfrak{d})$ are interpolated as

$$\begin{aligned}&\mathbf{u} \approx \mathbf{N}(\boldsymbol{\xi})\mathbf{d}; \quad \tilde{\mathbf{E}} \approx \mathbf{M}(\boldsymbol{\xi})\boldsymbol{\varsigma}; \quad \mathfrak{d} \approx \mathbf{N}(\boldsymbol{\xi})\tilde{\mathfrak{d}}; \quad \delta\mathbf{u} \approx \mathbf{N}(\boldsymbol{\xi})\delta\mathbf{d}; \\ &\delta\tilde{\mathbf{E}} \approx \mathbf{M}(\boldsymbol{\xi})\delta\boldsymbol{\varsigma}; \quad \delta\mathfrak{d} \approx \mathbf{N}(\boldsymbol{\xi})\delta\tilde{\mathfrak{d}}.\end{aligned}$$

Here, $\mathbf{M}(\boldsymbol{\xi})$ is so called enhancing interpolation matrix in the natural co-ordinates whose particular expression takes the form

$$\tilde{\mathbf{M}} = \begin{bmatrix} \xi^1 & 0 & 0 & 0 & 0 & 0 & 0 \\ 0 & \xi^1 & 0 & 0 & 0 & 0 & 0 \\ 0 & 0 & \xi^3 & \xi^1\xi^3 & \xi^2\xi^3 & 0 & 0 \\ 0 & 0 & 0 & 0 & 0 & \xi^1 & \xi^2 \\ 0 & 0 & 0 & 0 & 0 & 0 & 0 \\ 0 & 0 & 0 & 0 & 0 & 0 & 0 \end{bmatrix}. \tag{26}$$

The symbol $\boldsymbol{\varsigma}$ denotes the collection of EAS parameters. The transverse shear strains (E_{13}, E_{23} and transverse normal strain (E_{33}) are modified in line with ANS interpolation method to avoid transverse and trapezoidal locking. The interpolation of transverse shear are performed as in Fig. 1b using points (A, B,C,D) as

$$\begin{Bmatrix} E_{13}^{ANS} \\ E_{23}^{ANS} \end{Bmatrix} = \begin{Bmatrix} (1-\xi^2)E_{13}(\xi_A) + (1+\xi^2)E_{13}(\xi_C) \\ (1+\xi^1)E_{23}(\xi_B) + (1-\xi^1)E_{23}(\xi_D) \end{Bmatrix}. \tag{27}$$

and transverse normal strains using (E,F,G,H) as

$$E_{33}^{ANS} = \sum_{m=E,F,G,H} \frac{1}{4}\left(1+\xi_m^1\xi^1\right)\left(1+\xi_m^2\xi^2\right)E_{33}; \qquad \text{with } \xi_m^1, \xi_m^2 = \pm 1. \tag{28}$$

The gradient quantities such as displacement derived Green–Lagrangian strain $\mathbf{E}^u$, $\nabla_{\mathbf{x}}\mathfrak{d}$ and their variations are interpolated as

$$\mathbf{E}^u \approx \mathbf{B}(\mathbf{d})\mathbf{d}; \quad \delta\mathbf{E}^u \approx \mathbf{B}(\mathbf{d})\delta\mathbf{d}; \quad \nabla_{\mathbf{x}}\mathfrak{d} \approx \mathbf{B}^{\mathfrak{d}}(\mathbf{d})\tilde{\mathfrak{d}}, \quad \nabla_{\mathbf{x}}\delta\mathfrak{d} \approx \mathbf{B}^{\mathfrak{d}}(\mathbf{d})\delta\tilde{\mathfrak{d}} \quad ,$$

using the standard gradient operator $\mathbf{B}(\mathbf{d})$ and $\mathbf{B}^{\mathfrak{d}}(\mathbf{d})$.

For each pseudo increment $\Delta t := t_{n+1}^{(k)} - t_n > 0$, and assuming that $(\mathbf{u}, \tilde{\mathbf{E}}, \mathfrak{d})_{t_n}$ is known, the cumulative fatigue history reads

$$\bar{\alpha}_{t+1} = \bar{\alpha}_t + \int_{t_n}^{t_{n+1}} \dot{\bar{\alpha}}\mathrm{d}\tau = \bar{\alpha}_t + \Delta\bar{\alpha}, \tag{29}$$

where $\Delta\bar{\alpha}$ is approximated as

$$\Delta\bar{\alpha} = |\alpha_{n+1} - \alpha_n| H\left(\frac{\alpha_{n+1} - \alpha_n}{\Delta t}\right). \tag{30}$$

Moreover, following the standard finite element procedure, the residual equations in Eq. (25) in its discrete form are written as system of linear equations. See Appendix A for detailed computation of stiffness matrix.

The resulting system of linear algebraic equations in Eq. (A.7) is solved using the Newton solver. The detailed algorithm for the computational procedure is outlined in Algorithm 1. The Code for the computing starred components in the Algorithm 1 are presented in Appendix B.

Algorithm 1: Numerical Implementation Procedure

Data: $\mathbf{d}_n, \Delta\mathbf{d}_{n+1}^{(k)}, \mathfrak{d}_n, \Delta\mathfrak{d}_{n+1}^{(k)}$;
Result: $\mathbf{d}_{n+1}, \mathfrak{d}_{n+1}$;
Initialize: $\boldsymbol{\varsigma}_n, \mathbf{K}_{\boldsymbol{\varsigma}\mathbf{d},n}$;
while $||\mathcal{R}^{\mathbf{d}}||, ||\mathcal{R}^{\mathfrak{d}}|| > Tol$ **do**
  Compute $\Delta\boldsymbol{\varsigma}_{n+1}^{(k)} = -\left[\mathbf{K}_{\boldsymbol{\varsigma}\boldsymbol{\varsigma},n}\right]^{-1}\left[\mathbf{K}_{\boldsymbol{\varsigma}\mathbf{d},n}\Delta\mathbf{d}_{n+1}^{(k)}\right]$;
  Update the enhancing vector $\boldsymbol{\varsigma}_{n+1} = \boldsymbol{\varsigma}_n + \Delta\boldsymbol{\varsigma}_{n+1}^{(k)}$;
  for *each integration points* **do**
    Compute curvilinear basis vector $\mathbf{G}_{n+1,i}^{(k)}, \mathbf{g}_{n+1,i}^{(k)}$;
    Compute the shape functions $\mathbf{N}(\boldsymbol{\xi})_{n+1}^{(k)}$;
    Compute gradient operators $\mathbf{B}(\mathbf{d})_{n+1}^{(k)}$ and $\mathbf{B}^{\mathfrak{d}}(\mathbf{d})_{n+1}^{(k)}$;
    Modify the gradient operator according to ANS ;
    Compute the Green–Lagrangian strain tensor $\mathbf{E}_{n+1}^{(k)}$ according to Eq. (1) ;
    Compute elasticity tensor $\mathbb{C}_{n+1}^{(k)}$ according to Eq. (14);
    Compute PK2 Stress tensor $\mathbf{S}_{n+1}^{(k)}$ according to Eq. (1) ;
    if *stress split is used* **then**
      * Convert the PK2 Stress $\mathbf{S}_{n+1}^{(k)}$ into Cartesian coordinates $\hat{\mathbf{S}}_{n+1}^{(k)}$. ;
      * Compute Deformation gradient $\hat{\mathbf{F}}_{n+1}^{(k)}$ in Cartesian Coordinates ;
      Compute Cauchy Stress $\boldsymbol{\sigma}_{n+1}^{(k)}$ using Eq. (17) ;
      Compute principal stresses $\boldsymbol{\sigma}_{n+1,1}^{(k)}, \boldsymbol{\sigma}_{n+1,2}^{(k)}, \boldsymbol{\sigma}_{n+1,3}^{(k)}$ of the Cauchy stresses ;
    end
    Compute crack driving force using Eq. (18) or Eq. (13) ;
    Compute EAS Operator $\tilde{\mathbf{M}}_{n+1}^{(k)}$ according to Eq. (26) ;
    Compute the fatigue degradation function $f(\bar{\alpha})_{n+1}^{(k)}$ according to Eq. (22) or Eq. (23) ;
  end
  Compute elemental stiffness matrices from Eqs. (A.2)–(A.4) ;
  Compute the residual vectors from Eq. (25) ;
  Perform the static condensation procedure according to Eq. (A.7)
  Final Assembly
end

5. Virtual testing

The proposed fatigue fracture model based on the phase field method is evaluated in this section using several representative examples. The finite element formulation has been implemented into the general-purpose finite element software ABAQUS. These examples are categorized based on geometry, as described below.

First, a plate with a notch subjected to cycling loading is considered as an example of a linear model and for the comparison with the previous results. For this example, a driving force without split, as described in Eq. (A.5), is used. The fatigue effects on the plate with a notch under cyclic loading are analyzed for both low cycle and moderately high cycle fatigue. The crack growth against normalized cycles to failure is compared with [24].

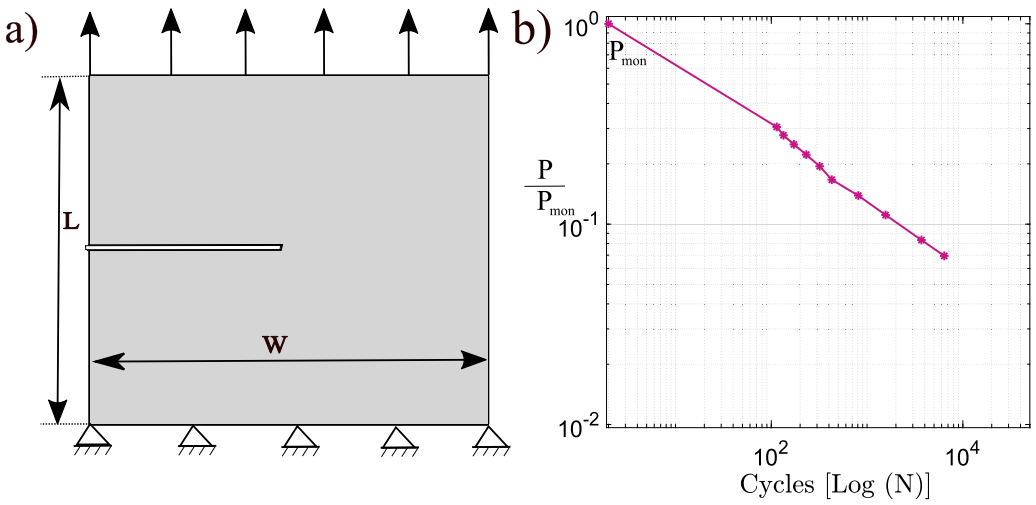

Fig. 2. (a) Geometry and, (b) modified SN curve.

Second, an example with a half-cylinder is investigated in order to explore the capabilities of shell structures, as the FE-model is prone to undergo several locking pathologies. As the fracture is predominantly dominated by Mode I failure, a driving force as described in Eq. (A.5) is employed.

Third, a pure mode-II shear example is considered to investigate the crack driving force arising from stress split, as in Eq. (A.6). As the fracture is dominated by mode-II fracture, it is also demonstrated that the driving force in Eq. (A.5) leads to mode-I fracture, resulting in a directional stress decomposition type model, which is also observed in [69]. Furthermore, the cyclic behavior of shear with stress split is examined in this example. The crack propagation with split and without split is compared to the results using [66].

A three-point bending example is considered to analyze the proposed model's ability to handle lockings in thin shells and cracks dominated by mixed-mode fractures. The results demonstrate that with the stress split, the solid shell can address this issue. Furthermore, it is shown that the same formulation can be employed for thick structures. In other words, the proposed model can be utilized as a regular solid element to analyze thick structures, as well as thin structures, even for examples such as bending without any locking phenomena. For the examples of Pure mode II shear and the three point bending example where tension–compression split is used, the load ratio of $R = 0$ is applied. Notice that, when the $R = -1$, due to the split, the compressive part of the strain energy does not add to the total accumulated strain energy. Refer [35] for more details.

Finally, the proposed model is utilized to analyze carbon fiber-reinforced composites (CFRC) through a dogbone specimen, utilizing the crack driving described in Eq. (A.6). Subsequently, the obtained numerical results are compared against the experimental data.

Note that throughout the article, the fatigue degradation function in Eq. (22) with $a = 2$ is used unless specified.

5.1. Notched plate

This example concerns with the application of the proposed model to notched plate specimen with a crack driving force as in Eq. (A.5). Fig. 2a) shows the sketch of the model with an initial notch length of 0.5 mm, length of $L = 1$ mm, width of w= 1 mm and thickness $h = 0.05$ mm. This example has been studied by considering alumina with Young's modulus $E = 210$ GPa, Poisson ratio $\nu = 0.3$, fracture energy of $\mathcal{G}_C = 2.7$ (N/mm), and the length scale $l = 0.024$ mm.

A cyclic displacement load with N number of cycles consisting of maximum P_{max} mm and minimum P_{min} mm is applied on the top surface, while the bottom surface is restrained. EAS and ANS are included in the whole domain but are turned off locally when the phase-field $\vartheta > 0.5$. Here, fatigue degradation function in Eq. (22) with $a = 2$ and the cumulative history variable independent of the mean load, is considered. In line with the example in [24], Fig. 4(a) shows the predicted crack extension vs. number of cycles for the variation of maximum amplitude. Notice that, as the maximum amplitude decreases, the number of cycles taken to failure increases. Also, as the maximum amplitude decreases, the number of cycles taken to start the nucleation also increases which is well reflected in Fig. 4(a). Being P_{mon} the amplitude required for the failure of the specimen under monotonic loading Fig. 2(b) shows the modified SN curve where the ratio of maximum load P and P_{mon} is plotted vs. the number of cycles in the log–log scale. It can be clearly seen that as the $\frac{P}{P_{mon}}$ ratio decreases, the number of cycles to failure increases. Generally, after $N = 10^7$, the specimen is considered to have an infinite life. In other words, in the sense of numerical approximations, there exists a threshold of $\frac{P}{P_{mon}}$ such that the specimen will have an infinite life. In other words, there exists a load amplitude such that the specimen under consideration will have infinite life. Based on Fig. 2(b), it is clear that for each load variation, a small difference in the load amplitude can have large change in the number of cycle (as an exponential functions) making the SN curve dense as the number of cycle increases.

The two dimensional model presented in [24] assumes a plane strain condition, while the proposed model is three dimensional and accounts for the specimen's thickness (very small). Hence, the dimensionless cycle number ($\frac{N}{N_u}$, for N_u being number of cycle at failure) versus crack extension between [24] and our model for different load amplitudes is compared and the results are presented in Fig. 3. It can be seen that the presented model predictions are in good agreement with the crack nucleation, propagation and failure.

Upon considering the variation of internal length scale l and keeping the maximum load amplitude $P_{max} = 0.0024$ constant, the crack extension vs. number of cycles are shown in Fig. 4(b). Complying with the idea of $\Gamma-$convergence, as the length scale decreases, the number of cycles required for failure increases. Moreover, it can be observed from Fig. 4(b) that variation of N for a linear variation of l is of exponential nature.

Fig. 5 shows the degraded energy and the phase-field values vs. number of cycles for $l = 0.0024$ mm and $P_{max} = 0.002$ mm at four different instances (A, B, C, D) which are equidistant from each other, with a distance approximately $(0.125, 0.25, 0.375, 0.5)$ mm from the notch tip. It can be seen from the energy degradation in Fig. 5(a) as the crack propagates, the bulk energy keeps decreasing until fracture. Moreover,

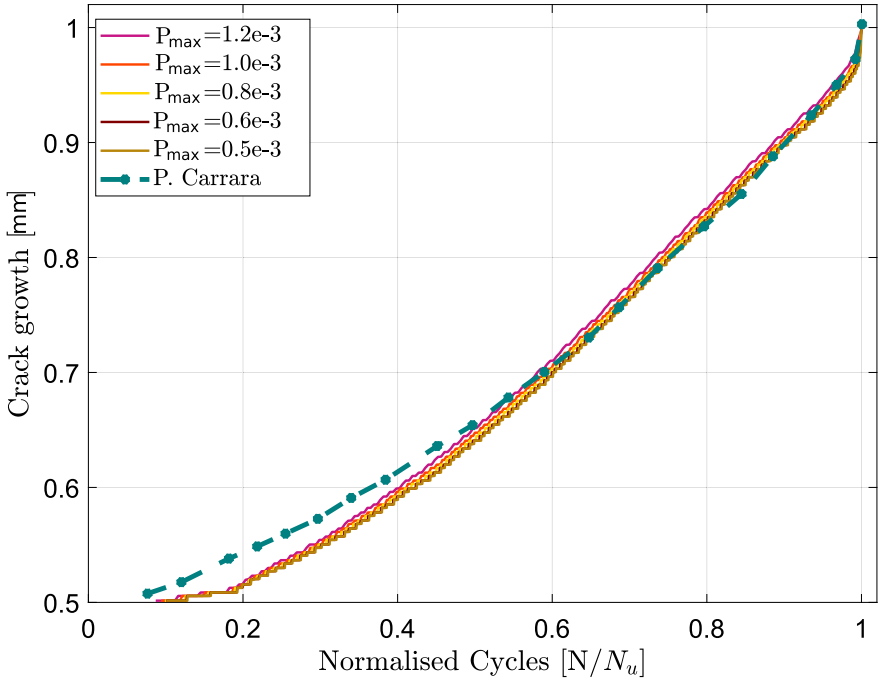

Fig. 3. Comparison of various load amplitude with the previous results [24] in 2D Plain strain.

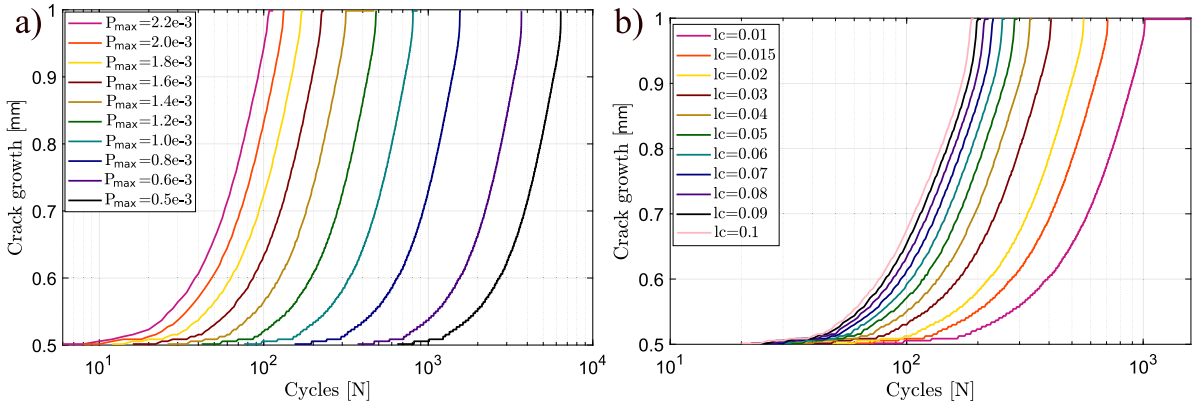

Fig. 4. Crack extension vs. number of cycles (N) (a) for different maximum load amplitude P and, (b) for different internal length scale l.

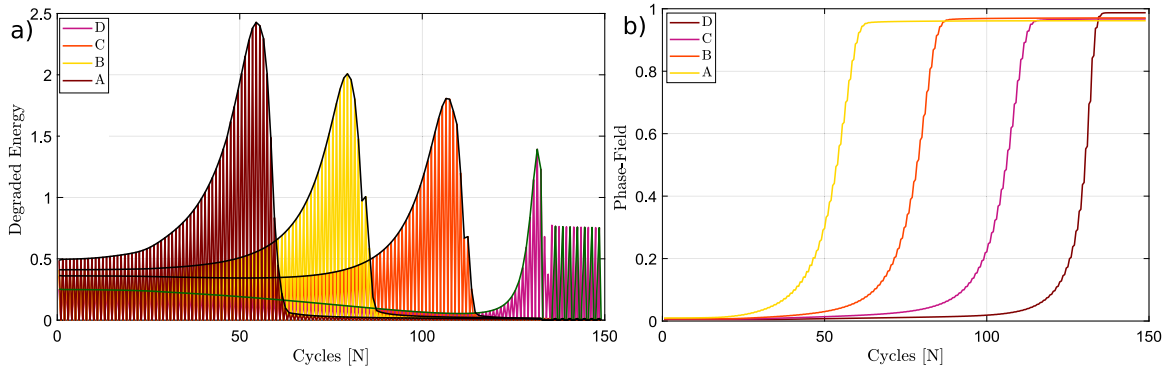

Fig. 5. (a) Degraded Energy vs. N and, (b) phase-field vs. N at points (A,B,C,D).

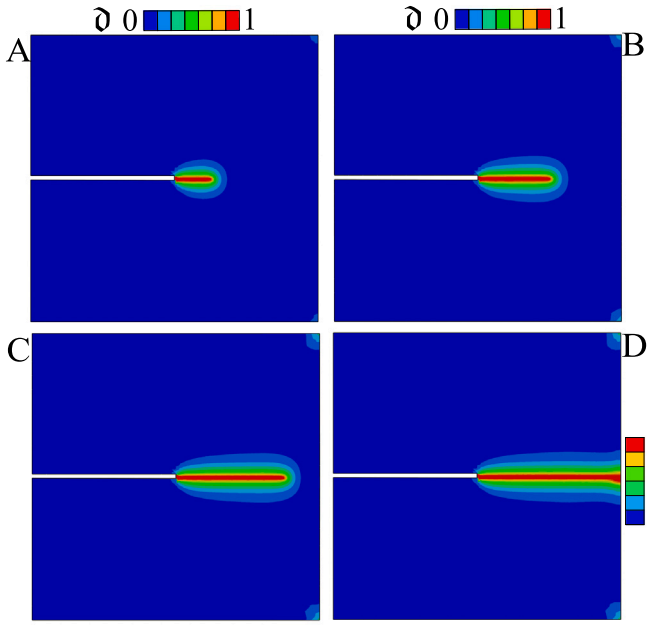

Fig. 6. Phase-field crack propagation up to points (A, B, C, D).

Fig. 5(b) shows the increase of phase-field at points (A, B, C, D) whose crack initiation, propagation and failure happens at different time instances. The crack propagation at the points (A, B, C, D) is depicted in Fig. 6 showing a stable crack propagation.

For the fatigue degradation function as in Eq. (23) (herein referred to as model-2), and a cumulative history variable mean-load independent, Fig. 7 shows the crack extension vs. number of cycles by varying the k parameter. It is observed that, for the $k < 0.26$, the crack propagation is stable resembling Model-1 (using Eq. (22)), whereas for $k > 0.26$, the crack nucleation is stable whereas the crack propagation becomes unstable, as shown in Fig. 7. This can be attributed to the fact that, the threshold of the fatigue function degradation is dependent on k in Eq. (23) making $f(\bar{\alpha}) = 0$ (symptotic). Moreover, as $k \to 0$, the number of cycles required for failure increases ($N \to \infty$).

5.2. Curved shells

In this example, a curved half cylindrical shell with a hole is considered. Geometrical description of the model considers a cylinder with a radius of $R = 2$ mm, length $L = 10$ mm, thickness $h = 0.01$ mm with an hole in the center with radius $r = 0.15$ mm. One axial end of the cylinder is fixed whereas the other axial end is loaded with N number of cycles of amplitude $(P, 0)$ is applied. The material properties are: Young's modulus $E = 210$ (GPa), Poisson ratio $\nu = 0.3$, fracture energy $\mathcal{G}_C = 2.7$ (MPa$\sqrt{\text{mm}}$) and the length scale $l = 0.2$ mm.

For the fatigue degradation function in Eq. (22) with $a = 2$, the crack extension vs. number of cycles for different load maximum load amplitude P is shown in Fig. 8(b), whereas the predicted SN curve is shown in Fig. 8(a). With the notation described in the previous example, as the load amplitude ($\Delta P = P$) decreases, the number of cycles N required for fracture increases. Also, it can be seen that the modified SN curve is dense, meaning that as the ratio of $\frac{P}{P_{mon}}$ ratio decreases, the number of cycles required for full fracture increases. Similar trends as plate with notch example in are observed for the curved shells. For $P_{max} = 2.4 \times 10^{-3}$ mm and $l = 0.2$ mm, Fig. 9 (top to bottom) shows the phase-field at cycles $N = 5000, 5500, 6000, 7500$ respectively showing a stable crack propagation.

5.3. Shear test

In this example, an application of spectral stress split on mode II shear is investigated. In particular, the Cauchy stress is computed from the (second Piola-Kirchhoff) PK2 stress tensor via transformation of curvilinear co-ordinate to Cartesian. Later, a spectral decomposition of the Cauchy stresses is computed in order to distinguish between positive and negative part of the stress. The crack driving force is then computed using the positive part of the Cauchy stress.

The body under consideration contains a plate with a notch whose length (L) and width (w) are L=w= 1mm, and the thickness of 0.05 mm. Displacement boundary condition at the top surface in y-direction is applied with an unrestricted movement in the x- and z-direction, whereas the bottom plate is fully restrained to simulate the mode II shear test as in Fig. 10(a).

Apart from the Cauchy-based stress split that was discussed, splits based on the second Piola–Kirchhoff tensor and alternatively strain splits based on either the Euler–Almansi or the Green–Lagrange strains can be adopted. However, as noted in [69], stain-based splits can lead to unphysical results. This can be attributed to the fact that a significant amount of shear stress is transmitted over the crack at the corner, resulting in either an under-estimation or over-estimation of the reaction forces. In addition to the rational Cauchy-based split, the model was also tested with a strain-based split. It was observed that, in the strain-based split and without any split, instead of predicting the kinking of the crack towards the corner, the crack propagated straight, resulting in a crack similar to that in mode I. This is consistent with the literature referred to as a "directional split" [69], which is considered unphysical. For the purpose of comparison, the crack propagation results are presented in Fig. 12 for three cases: (i) without stress split, (ii) with Cauchy-based stress split, and (iii) using a two-dimensional plane strain problem with spectral split, as defined in [66].

This example is analyzed by considering alumina with Young's modulus $E = 210$ GPa, Poisson ratio $\nu = 0.3$, fracture energy of $\mathcal{G}_C = 2.7$ MPa$\sqrt{\text{mm}}$, and the length scale $l = 0.07$ mm. For the monotonic loading, Fig. 11 presents the force vs. displacement curve along with the crack propagation for Cauchy based split. Crack propagation at each of the instances (A, B, C, D) of the reaction curve is also presented.

Equipped with the result based on the monotonic loading, the specimen is tested for a cyclic loading with load ranging from zero to amplitude of P over N cycles. Fig. 13(a) presents the crack extension vs. number of cycle for different load amplitudes P. It can be seen that as the load amplitude decreases, the number of cycles to fracture increases. Moreover, Fig. 10(b) presents the predicted SN curve in semi-log plot. It is clearly observed that SN curve is dense and as the ratio of $\frac{P}{P_{mon}}$ ratio decreases, the number of cycles required for full fracture increases. Furthermore, Fig. 13(b) represents the phase-field at different points (A,B,C,D) corresponding to the position of crack tip in Fig. 11 for cyclic loading with load amplitude $P = 20 \times 10^{-4}$.

5.4. Three-point bending test with initial notch

The rational behind this example is twofold, (a) the presented solid-shell can be used as a solid element alternative with energy split, (b) to demonstrate the fatigue effects in the three point symmetric in-plane bending with asymptotic crack degradation. Within the context of configurational force driven crack propagation, a simply supported notched beam with dimension as shown in Fig. 14(a) is considered. A symmetric loading is applied with two edges restrained as shown in Fig. 14(a). The model is discritised with five elements in the thickness direction representing a thick plate.

As in Section 5.3, crack driving force is computed using the Cauchy based stress split. Fig. 15 represents the force vs. displacement and the crack extension vs. displacement for a monotonic loading condition. It can be seen that due to load application, crack extension in the starting is faster, and as the crack extends towards the load application point, an

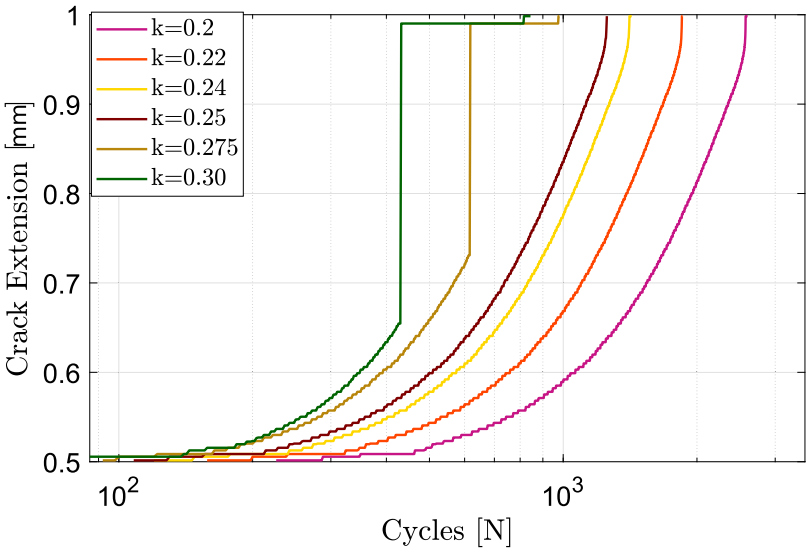

Fig. 7. Crack Extension using the fatigue degradation function defined in Eq. (23) (defined as model-2) for the variation of k in Eq. (23).

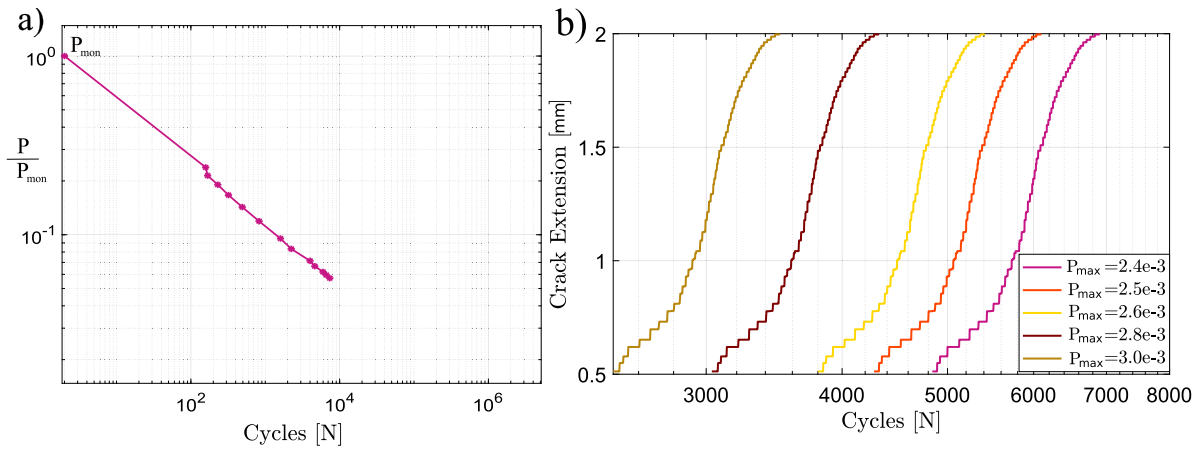

Fig. 8. (a) SN Curve and, (b) Crack extension vs. number of cycles for cylindrical shells.

asymptotic crack propagation behavior can be observed. Numerically, it can also be noticed that there exists a crack extension value (denoted as C_T) such that the reaction forces shows meta-stable behavior. i.e for the crack extension Ac and reaction force R_τ at time step τ, there exists a value $Ac = C_T$, such that if $Ac > C_T$, $R_\tau - R_{\tau+1} \to 0$. Note that, in the fatigue case, C_T is chosen as 25 based on Fig. 15. Meaning that, if the crack extension reached a value of $C_T = 25$, the model is considered to be failed.

In order to understand the effect of characteristic length scale l_c on the asymptotic crack propagation behavior, three different length scales are considered with $l_c = 0.07, 0.05, 0.03$ mm. In the related literature, characteristic length scale is characterized by strength of material [70]. In that case, the variation of the length scale can be treated as a change of strength of material due to different types of material hardening process. For each length scale, different numerical experiments with different amplitude are conducted in order to obtain a comprehensive understand of the fatigue behavior. Fig. 14(b) presents the modified SN curve for the different length scale. For a comprehensive understanding, Fig. 14(b) left represents the modified SN curve, whereas Fig. 14(b) right) represents the maximum reaction force vs number of cycle. It is observed that in the modified SN curve, the variation of length scale is almost constant, whereas the difference can be observed distinctly when absolute values of the maximum reaction are plotted. As in the previous examples, as the ratio of $\frac{P}{P_{mon}}$ ratio decreases, the number of cycles required for fracture increases.

Crack extension vs. number of cycles for different load amplitude for a constant length scale $l_c = 0.07$ mm is presented in Fig. 16(a), whereas Fig. 16(b) represents the variation of length scale over a constant load amplitude of Amp $= 0.09$ mm. It can be observed that as the load amplitude decreases, the number of cycles taken for fracture increases. On the contrary, as the strength increases (length scale decreases), the number of cycles required to fracture also increases. Numerically, this can also be taken as the $\Gamma-$convergence for the proposed model.

In order to present the fatigue degradation effects, Fig. 17 is considered. The fatigue degradation of the models with length scale $l_c = 0.07$ mm and with load amplitude of $Amp = 0.6$ mm, and $Amp = 0.8$ mm is considered. Notice that, as the load amplitude increases, the maximum reaction force also increases. Fig. 17 also presents the crack extension curve for the load amplitude of $Amp = 0.06$ mm. With this, three red lines with crack extension with 10 mm (A), 15 mm(B), and 25 mm (C) is presented, whose corresponding crack propagation are shown in Fig. 17. Notice that as the crack extension threshold C_T (here $C_T = 25$ mm) is reached, the reaction forces are small and almost constant.

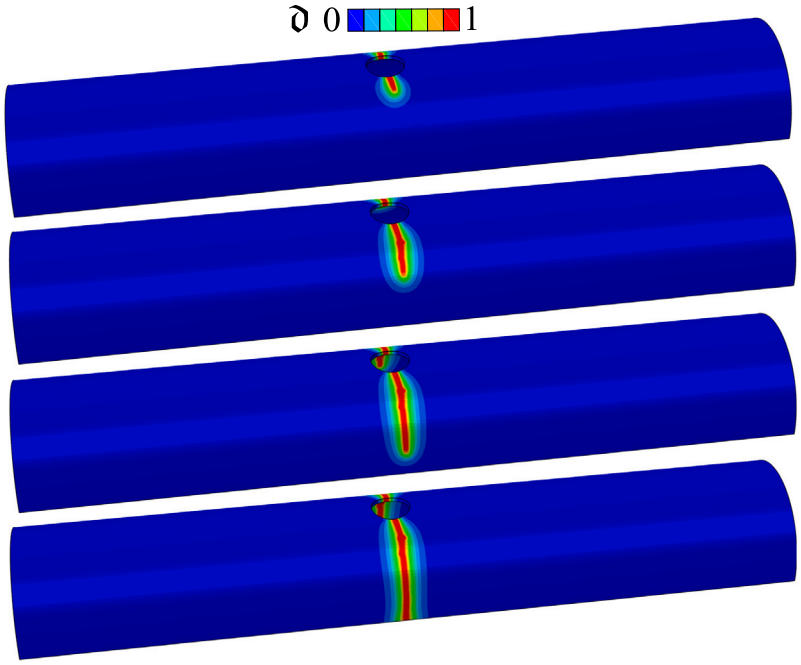

Fig. 9. (a) Phase-field crack propagation for cylindrical shell.

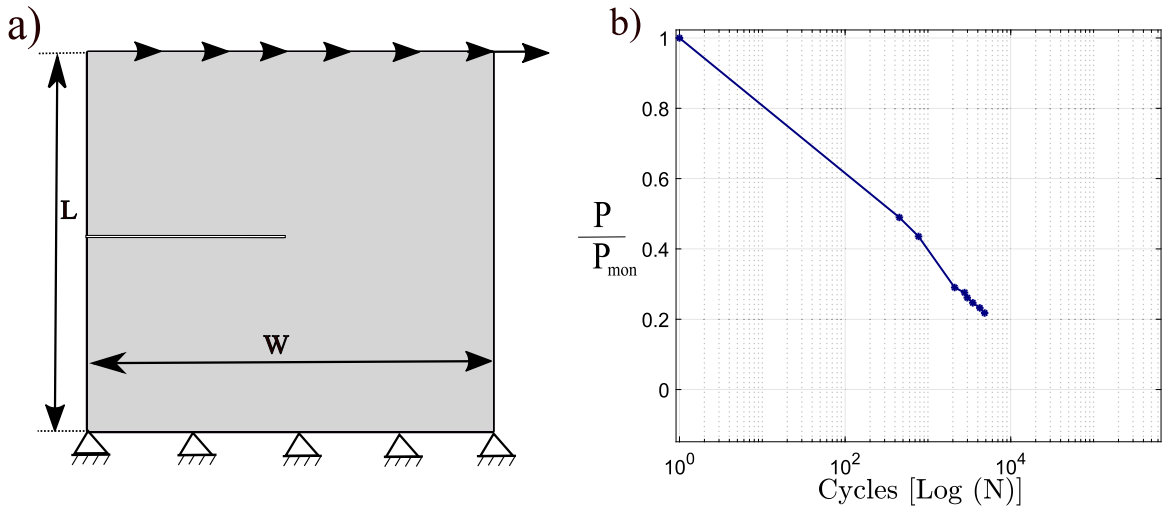

Fig. 10. (a) Geometry and, (b) Modified SN curve for Cauchy based model.

5.5. Layered composites

This example showcases the application of the proposed model to analyze the fatigue behavior of carbon fiber-reinforced composites (CFRCs) using a dogbone specimen with a driving force, as described in Eq. (A.6). The geometrical description of the model is depicted in Fig. 18(a), with a thickness of $h = 2.28$. In article, Benedikt et al. [72] conducted experiments on the fatigue behavior of thin and thick ply composites using computer tomography. The experiments involved a unidirectional system of CFRC composed of epoxy resin TP402 and T700S carbon fibers to produce plies with a target fiber volume content of 55% and a fiber area weight of 30 gsm, 60 gsm, 120 gsm, 240 gsm and 360 gsm. Standard dogbone specimens with a gauge length of 130 mm and a gauge width of 21 mm (except for 30 gsm) were milled from these plies, and each model was subjected to uniaxial loads to determine its compressive/tensile strength and corresponding stress–strain curves. Fatigue tests were conducted for tension–tension, tension–compression, and compression–compression tests. For the tension–tension test, a minimum to maximum load ratio of $R = 0.1$ was applied, and the stress amplitude was plotted for various numbers of cycles. To analyze the damage and possible crack growth, the samples were stopped at 0, 5×10^4, 3×10^5, and 8×10^5 cycles, and the results were examined using computer tomography. For more information on the experimental setup, sample preparation, and analysis techniques, readers are referred to [72].

In the sequel, we focus the attention on one particular case corresponding to the sample with 60 gsm and subjected to a fatigue load corresponding to tension–tension with a load ratio of $R = 0.1$. The tensile strength of this sample is estimated to be between 950–1050 Mpa based on the results of the uni-axial tension tests reported in Fig 3 of [72]. The static loading experiment is employed for the validation of the current formulation and for the calibrating of the fracture toughness of the sample which due to the lack of reliable data can be estimated as $Gc = 5$–10 N/mm based on the target fiber

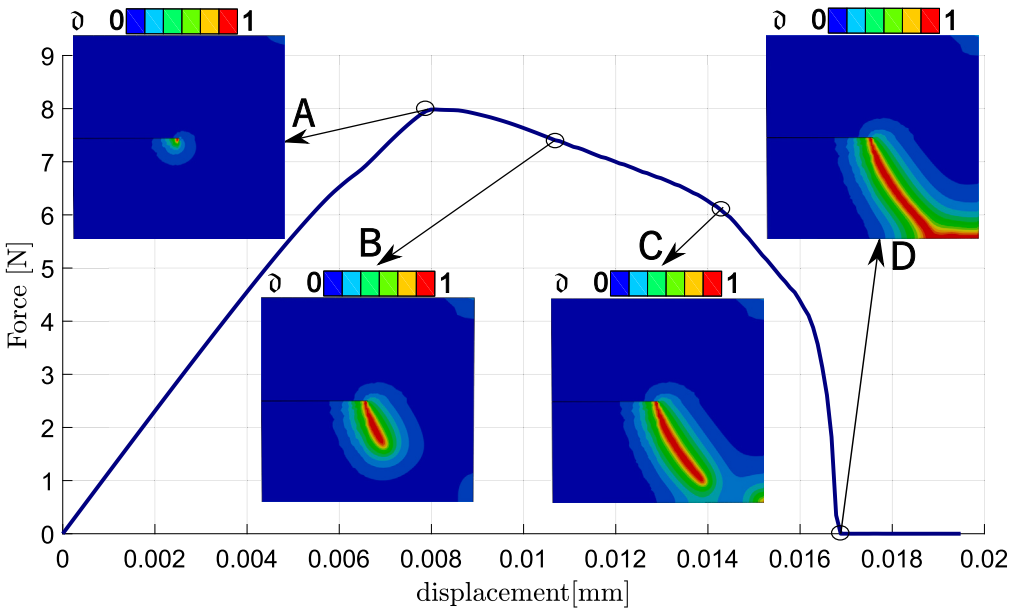

Fig. 11. Force vs. displacement curve with Cauchy-based split under monotonic loading.

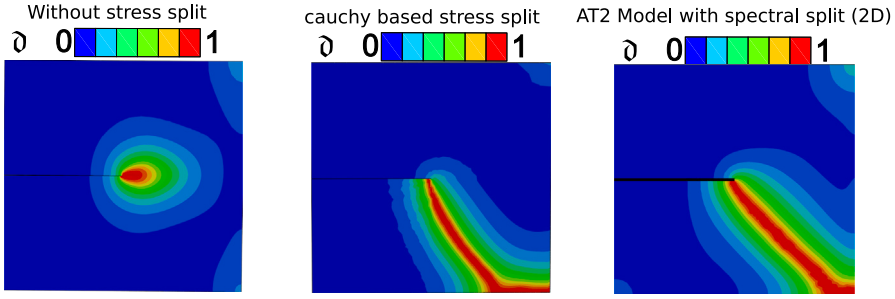

Fig. 12. Comparison of the shear test without stress split in thin shells, with Cauchy-based stress split, and AT2 Model with spectral split (in-plane strain) as in [66].

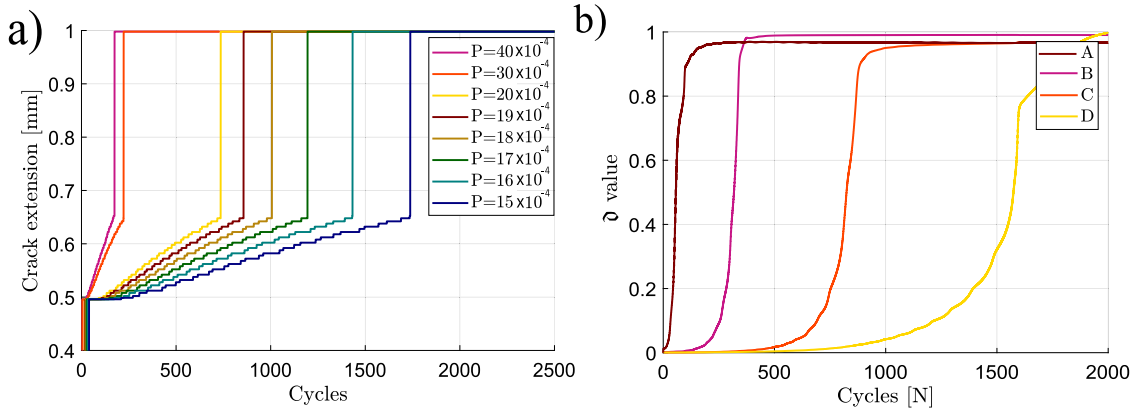

Fig. 13. (a) Crack extension vs. number of cycles for shear test in both Cauchy (Solid line), (b) Phase-field vs. N at points (A,B,C,D).

volume and fiber areal weight as presented in [73]. The characteristic length scale required for the phase field model can be estimated as l_c = 0.30–0.38 mm based on the apparent tensile strength. For the numerical experiments, the average values of all parameters are used.

The model presented in Fig. 18(a) is subjected to a displacement-controlled fatigue load with a ratio of minimum to maximum displacement of R = 0.1, as shown in Fig. 18(b). The resulting stress amplitude and the number of cycles to failure are recorded for Gc = 10 N/mm, with power a = 2, and Gc = 5 N/mm with power a = 1.25 in Eq. (22). These results are plotted against the experimental data in Fig. 18(c). The upper pink line represents the suggested SN curve with 50% suggested in the experiments. The numerical results in the low cycle regime show good agreement with the experimental results, especially considering the uncertainties of the experimental data. It is also observed that as the power of the fatigue degradation function decreases (below 2), the numerical SN curve tends to be steeper. Additionally, an increase in Gc shifts the SN curve rightwards in Fig. 18(c).

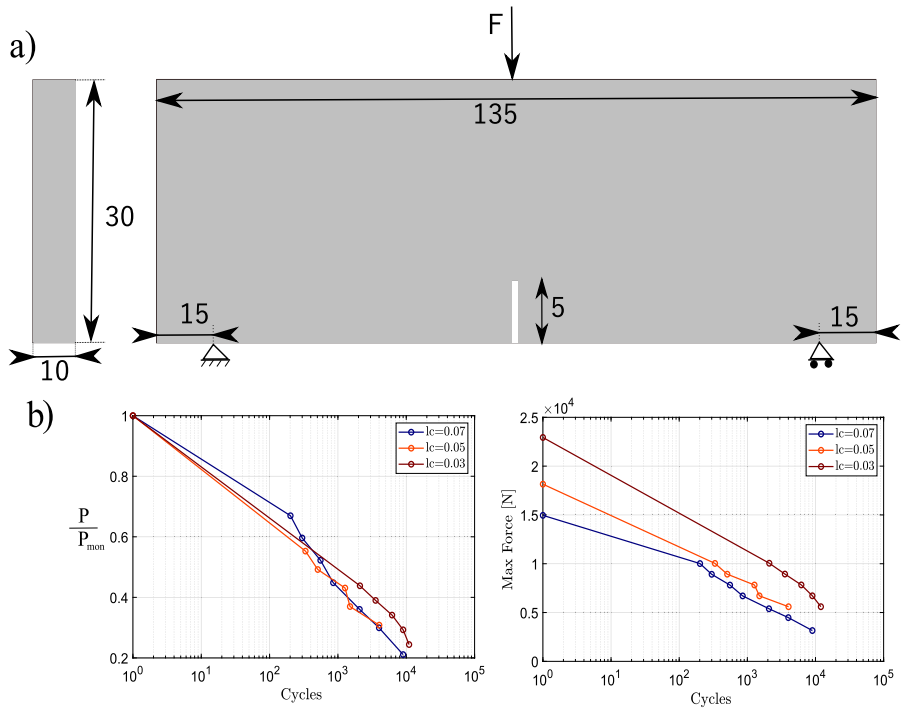

Fig. 14. (a) Geometrical description of model. (b) Modified SN curve and max reaction force vs. number of cycle.

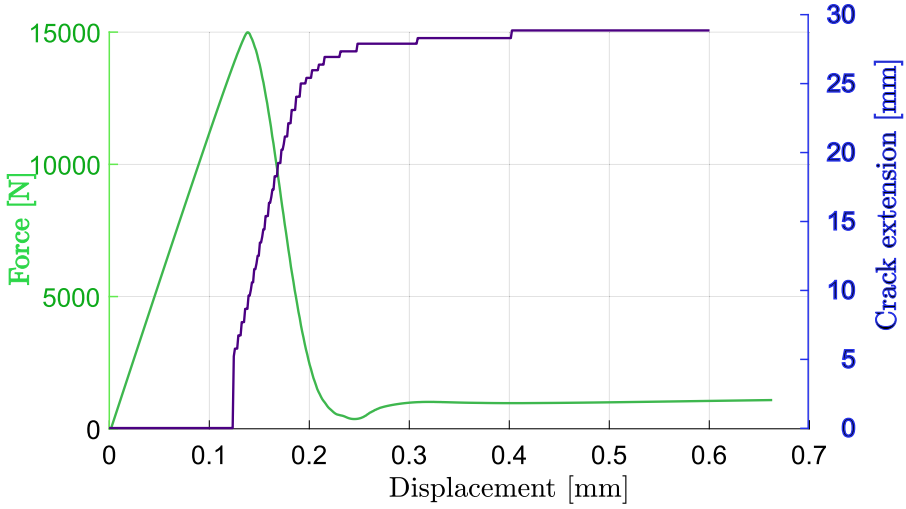

Fig. 15. (a) Force vs. displacement vs. crack extension in monotonic loading for Cauchy–based stress split.

6. Conclusions

A phase-field fracture model has been proposed for the analysis of structures subjected to fatigue loading using locking-free solid shell finite elements with full integration. For the sake of realistic fracture prediction, the computation of the crack driving force has been based on the positive/negative Cauchy stress split and the fatigue effect has been included via a degradation of the fracture toughness, and the differences highlighted.

The finite element treatment has been described in details and modularly implemented in the general-purpose finite element software ABAQUS. Several numerical examples were analyzed in order to assess the predictive capability of the proposed fatigue fracture model considering different splits, namely; plate with a notch, curved shell, mode II shear, and three-point bending. The proposed model has been demonstrated to be suitable for homogenized fiber-reinforced composites, and the numerical results have been compared with experimental observations.

In conclusion, the presented model has been shown to be a reliable tool for predicting fracture and fatigue events in thin-walled structures including laminates. There are several opportunities for further research that can be built on the model, such as developing more advanced phase field models for fatigue that take into account the effects of microstructure and the evolution of damage at the microscale, incorporating other types of loading, such as thermal and thermo-mechanical loading, and examining the effects of different material properties on the fatigue behavior of solid shells. Overall, the use of phase field methods entails the potential of providing valuable insights into the underlying mechanisms of fatigue and to support the development of more accurate and efficient numerical models for predicting the durability of structures.

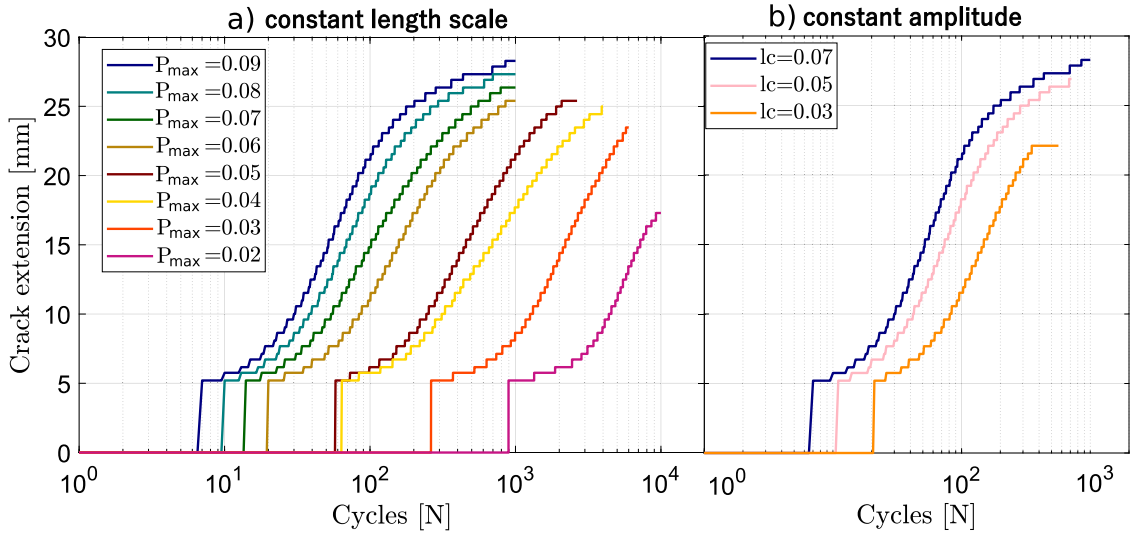

Fig. 16. (a) Crack extension vs. number of cycle for $l_c = 0.07$ (b) Crack extension vs. Number of cycle for constant load amplitude Amp = 0.09.

Declaration of competing interest

The authors Pavan Kumar Asur VK, Aamir Dean, Jose Reinoso, Heinz Pettermann, Marco Paggi declare that they have no known competing financial or personal relationships that could have appeared to influence the work reported in this paper.

Data availability

The Abaqus codes associated with the paper can be downloaded from the following link "https://github.com/Pavan-asur/Fatigue-Solid shell". Additional data will be made available on request.

Acknowledgments

MP would like to acknowledge funding from the Italian Ministry of University and Research to the Research Project of National Interest PRIN 2017 "XFAST-SIMS: Extra fast and accurate simulation of complex structural systems" (MUR code 20173C478N).

JR is grateful to the financial support of Ministerio de Ciencia e Innovación (Projects TED2021-131649B-I00 and PID2019-109723GB-I00) and the funding received from the European Union's Horizon 2020 research and innovation program under the Marie Sklodowska-Curie grant agreement No. 101086342 – Project DIAGONAL (Ductility and fracture toughness analysis of functionally graded materials; HORIZON-MSCA-2021-SE-01 action)

Appendix A. Stiffness matrix derivation

Following the standard finite element procedure, the residual equations in Eq. (25) in its discrete form are written as system of linear equations as

$$\begin{bmatrix} \mathbf{K}_{\mathbf{dd}} & \mathbf{K}_{\mathbf{d}\varsigma} & \mathbf{K}_{\mathbf{d}\tilde{\mathfrak{d}}} \\ \mathbf{K}_{\varsigma\mathbf{d}} & \mathbf{K}_{\varsigma\varsigma} & \mathbf{K}_{\varsigma\tilde{\mathfrak{d}}} \\ \mathbf{K}_{\tilde{\mathfrak{d}}\mathbf{d}} & \mathbf{K}_{\tilde{\mathfrak{d}}\varsigma} & \mathbf{K}_{\tilde{\mathfrak{d}}\tilde{\mathfrak{d}}} \end{bmatrix} \begin{bmatrix} \Delta\mathbf{d} \\ \Delta\varsigma \\ \Delta\tilde{\mathfrak{d}} \end{bmatrix} = \begin{bmatrix} \hat{\mathcal{R}}^{u}_{\text{ext}} \\ \mathbf{0} \\ \mathbf{0} \end{bmatrix} - \begin{bmatrix} \hat{\mathcal{R}}^{u}_{\text{int}} \\ \hat{\mathcal{R}}^{\varsigma}_{\text{int}} \\ \hat{\mathcal{R}}^{\tilde{\mathfrak{d}}}_{\text{int}} \end{bmatrix}. \tag{A.1}$$

The components of stiffness matrix reads

$$\mathbf{K}_{\mathbf{dd}} = \int_{\mathcal{B}_0} g(\mathfrak{d}) \left(\mathbf{B}(\mathbf{d})^{\mathrm{T}} \mathbb{C} \mathbf{B}(\mathbf{d}) + \left[\frac{\partial \mathbf{B}(\mathbf{d})}{\partial \mathbf{d}} \right]^{\mathrm{T}} \mathbf{S} \right) \mathrm{d}\Omega = \mathbf{K}_{\mathbf{dd},\text{mat}} + \mathbf{K}_{\mathbf{dd},\text{geom}}$$

$$\mathbf{K}_{\mathbf{d}\varsigma} = \int_{\mathcal{B}_0} g(\mathfrak{d}) \mathbf{M}(\boldsymbol{\xi})^{\mathrm{T}} \mathbb{C} \mathbf{B}(\mathbf{d}) \, \mathrm{d}\Omega; \quad \mathbf{K}_{\mathbf{d}\tilde{\mathfrak{d}}} = \int_{\mathcal{B}_0} -2(1-\mathfrak{d}) \mathbf{B}(\mathbf{d})^{\mathrm{T}} \mathbf{S} \mathbf{N}(\boldsymbol{\xi}) \, \mathrm{d}\Omega,$$

$$\mathbf{K}_{\varsigma u} = \int_{\mathcal{B}_0} g(\mathfrak{d}) \mathbf{M}(\boldsymbol{\xi})^{\mathrm{T}} \mathbb{C} \mathbf{B}(\mathbf{d}) \, \mathrm{d}\Omega; \quad \mathbf{K}_{\varsigma\varsigma} = \int_{\mathcal{B}_0} g(\mathfrak{d}) \mathbf{M}(\boldsymbol{\xi})^{\mathrm{T}} \mathbb{C} \mathbf{M}(\boldsymbol{\xi}) \, \mathrm{d}\Omega,$$
$$\mathbf{K}_{\varsigma\tilde{\mathfrak{d}}} = \int_{\mathcal{B}_0} -2(1-\mathfrak{d}) \mathbf{M}(\boldsymbol{\xi})^{\mathrm{T}} \mathbf{S} \mathbf{N}(\boldsymbol{\xi}) \, \mathrm{d}\Omega; \tag{A.3}$$

$$\mathbf{K}_{\tilde{\mathfrak{d}}\mathbf{d}} = \int_{\mathcal{B}_0} -2(1-\mathfrak{d}) \mathbf{N}(\boldsymbol{\xi})^{\mathrm{T}} \mathbf{S} \mathbf{B}(\mathbf{d}) \, \mathrm{d}\Omega; \quad \mathbf{K}_{\tilde{\mathfrak{d}}\varsigma} = \int_{\mathcal{B}_0} -2(1-\mathfrak{d}) \mathbf{N}(\boldsymbol{\xi})^{\mathrm{T}} \mathbf{S} \mathbf{M}(\boldsymbol{\xi}) \, \mathrm{d}\Omega,$$
$$\mathbf{K}_{\tilde{\mathfrak{d}}\tilde{\mathfrak{d}}} = \int_{\mathcal{B}_0} \left[2f(\bar{\alpha}(t)) \frac{G_C}{l} \mathcal{H} \right] \mathbf{N}(\boldsymbol{\xi})^{\mathrm{T}} \mathbf{N}(\boldsymbol{\xi}) \, \mathrm{d}\Omega + \int_{\mathcal{B}_0} 2f(\bar{\alpha}(t)) G_C l \mathbf{B}^{\mathfrak{d}}(\boldsymbol{\xi})^{\mathrm{T}} \mathbf{B}^{\mathfrak{d}}(\boldsymbol{\xi}) \, \mathrm{d}\Omega, \tag{A.4}$$

with crack driving force $\mathcal{H}$ takes the form

$$\mathcal{H} = \max_{\tau \in [0,t]} \left[\Psi(\mathbf{u}, \tilde{\mathbf{E}}) \right]. \tag{A.5}$$

In the case while using the stress split, the crack driving force is modified to be only positive part of the maximum strain energy computed via Eq. (18) i.e

$$\mathcal{H} = \max_{\tau \in [0,t]} \left[\Psi^{+}(\mathbf{u}, \tilde{\mathbf{E}}) \right]. \tag{A.6}$$

Due to inter-element continuity of the enhanced strains, the above system of linear equation can be condensed via standard static condensation process as

$$\begin{bmatrix} \mathbf{K}^{*}_{\mathbf{dd}} & \mathbf{K}^{*}_{\mathbf{d}\tilde{\mathfrak{d}}} \\ \mathbf{K}^{*}_{\tilde{\mathfrak{d}}\mathbf{d}} & \mathbf{K}^{*}_{\tilde{\mathfrak{d}}\tilde{\mathfrak{d}}} \end{bmatrix} \begin{bmatrix} \Delta\mathbf{d} \\ \Delta\tilde{\mathfrak{d}} \end{bmatrix} = \begin{bmatrix} \tilde{\hat{\mathcal{R}}}^{\mathbf{d}} \\ \tilde{\hat{\mathcal{R}}}^{\tilde{\mathfrak{d}}} \end{bmatrix} \tag{A.7}$$

where $\mathbf{K}^{*}_{ij} = \mathbf{K}_{ij} - \mathbf{K}_{i\varsigma}\mathbf{K}^{-1}_{\varsigma\varsigma}\mathbf{K}_{\varsigma j}$ and $\tilde{\hat{\mathcal{R}}}^{j} = \mathcal{R}^{j}_{ext} - \mathcal{R}^{j}_{int} + \mathbf{K}_{i\varsigma}\mathbf{K}^{-1}_{\varsigma\varsigma}\mathcal{R}^{\varepsilon}_{int}$ for each $i, j = \{\mathbf{d}, \tilde{\mathfrak{d}}\}$. The resulting final equations can be solved using an staggered scheme.

Appendix B. FORTRAN codes for computing driving force

B.1. Convert the PK2 stress $\mathbf{S}^{(k)}_{n+1}$ into Cartesian coordinates $\hat{\mathbf{S}}^{(k)}_{n+1}$

The following subroutine uses Covariant basis in the curvilinear coordinates to transform the stress from curvilinear to cartesian coordinates

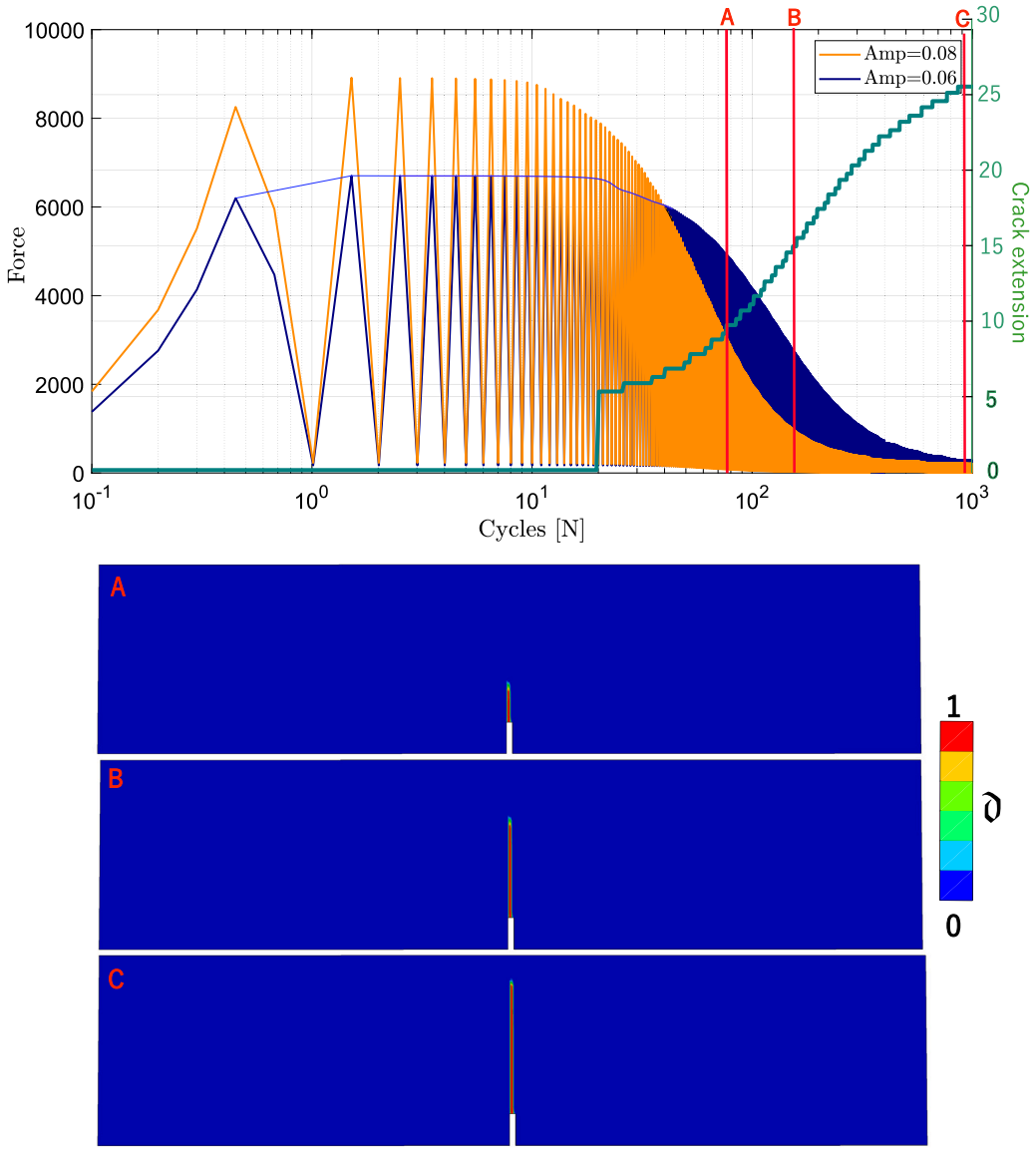

Fig. 17. (a) Force vs. number of cycle for fatigue loading along with crack propagation at points (A,B,C) for $l = 0.07$ and load amplitude of Amp = 0.06.

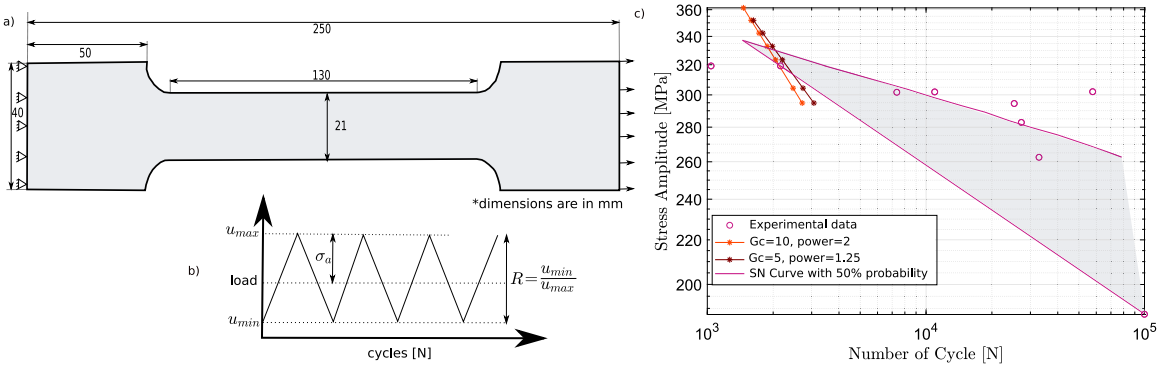

Fig. 18. (a) Geometry and boundary conditions, (b) applied load in tension–tension, (c) comparison between experimental data and numerical predictions.

```
subroutine s8_kon_cuca(PK2curv,PK2_cart,gkovr)
  implicit none
     INTEGER i,j
     REAL*8 PK2curv(3,3), Tcur(3,3),PK2_cart(3,3),
     gkovr(3,3)
    Tcur(:,:)=0.d0 !Define Tcur Variable to be zerp
    PK2_cart(:,:)=0.0d0 !PK2 Stress in cartisian
    Coordinates
    Tcur(:,:)=PK2curv(:,:) !Now Tcur is the Stress in
    Curvilinear coordinates
! gkovr is the  Covariant basis  in reference
configuration
 do i=1,3
  do j=1,3
   PK2_cart(1,1)=PK2_cart(1,1)+gkovr(1,i)*
   gkovr(1,j)*Tcur(i,j)
   PK2_cart(1,2)=PK2_cart(1,2)+gkovr(1,i)*
   gkovr(2,j)*Tcur(i,j)
   PK2_cart(1,3)=PK2_cart(1,3)+gkovr(1,i)*
   gkovr(3,j)*Tcur(i,j)
   PK2_cart(2,2)=PK2_cart(2,2)+gkovr(2,i)*
   gkovr(2,j)*Tcur(i,j)
   PK2_cart(2,3)=PK2_cart(2,3)+gkovr(2,i)*
   gkovr(3,j)*Tcur(i,j)
   PK2_cart(3,3)=PK2_cart(3,3)+gkovr(3,i)*
   gkovr(3,j)*Tcur(i,j)
  end do
 end do

!PK2_cart is the stress in cartesian coordinates
 return
 end
```

B.2. Compute deformation gradient $\hat{\mathbf{F}}_{n+1}^{(k)}$ in Cartesian coordinates

The following subroutine computes the deformation gradient in Cartesian coordinates using covariant basis vector in current configuration and contravariant basis in reference configuration

```
      subroutine kDefGradient(F,JacobF,Finv,gkovc,
      gkonr)
       implicit none
!Subroutine to compute the shape functions and ther
derivatives
     INTEGER i,j,k,l
     REAL*8 F(3,3),JacobF,Finv(3,3),gkovc(3,3),
     gkonr(3,3)
     !initialization
 F(:,:)=0.0d0 !deformation gradient
 Finv(:,:)=0.0d0 !inverse of deformation gradient
 JacobF = 0.d0 !Jacobian of the deformation gradient
! gkovc is the covariant basis in current configuration
!  gkonr is the contravariant basis in reference
configuration
     do i=1,3
       do j=1,3
        do k=1,3
        F(j,i) =  F(j,i) + gkovc(i,k)*gkonr(j,k);
        enddo
       enddo
     enddo
  JacobF = F(1,1)*F(2,2)*F(3,3)+
   * F(1,3)*F(2,1)*F(3,2)+ F(3,1)*F(1,2)*F(2,3) -
   *    F(3,1)*F(2,2)*F(1,3)-F(3,3)*F(1,2)*F(2,1)-
   *    F(1,1)*F(2,3)*F(3,2)
    if(JacobF.gt.0.0d0) then
   Finv(1,1)= (F(2,2) *F(3,3) - F(3,2) *F(2,3))/
   JacobF
   Finv(1,2)= -(F(1,2) *F(3,3) - F(1,3) *F(3,2))/
   JacobF
    Finv(1,3)= (F(1,2) *F(2,3) - F(2,2) *F(1,3))/
    JacobF
   Finv(2,1)= -(F(2,1) *F(3,3) - F(3,1) *F(2,3))/
   JacobF
   Finv(2,2)= (F(1,1) *F(3,3) - F(1,3) *F(3,1))/
   JacobF
   Finv(2,3)= -(F(1,1) *F(2,3) - F(2,1) *F(1,3))/
   JacobF
   Finv(3,1)= (F(2,1) *F(3,2) - F(3,1) *F(2,2))/
   JacobF
   Finv(3,2)= -(F(1,1) *F(3,2) - F(3,1) *F(1,2))/
   JacobF
   Finv(3,3)= (F(1,1) *F(2,2) - F(1,2) *F(2,1))/
   JacobF
   endif

 return
    end
```

References

[1] P. Eisenlohr, E. Santecchia, A.M.S. Hamouda, F. Musharavati, M. Cabibbo, S. Spigarelli, A review on fatigue life prediction methods for metals, Adv. Mater. Sci. Eng. 2016 (2016) 1687–8434.

[2] A. Wohler, Über die festigkeitsversuche mit eisen und stahl, 1870.

[3] P. Paris, F. Erdogan, A critical analysis of crack propagation laws, J. Basic Eng. 85 (1963) 528–533.

[4] P.C. Paris, A rational analytic theory of fatigue, 1961.

[5] L.F. Coffin Jr., A study of the effects of cyclic thermal stresses on a ductile metal, Trans. Am. Soc. Mech. Eng. 76 (2022) 931–949.

[6] S.S. Manson, Behavior of materials under conditions of thermal stress, 1953.

[7] M. Ciavarella, M. Paggi, A. Carpinteri, One, no one, and one hundred thousand crack propagation laws: A generalized Barenblatt and Botvina dimensional analysis approach to fatigue crack growth, J. Mech. Phys. Solids 56 (2008) 3416–3432.

[8] N. Hou, Z. Wen, Q. Yu, Z. Yue, Application of a combined high and low cycle fatigue life model on life prediction of SC blade, Int. J. Fatigue 31 (2009) 616–619.

[9] A. Palmgren, The service life of ball bearing, Z. Ver. Dtsch. Ing (1924) 339–341.

[10] M.A. Miner, Cumulative damage in fatigue, J. Appl. Mech. 12 (2021) A159–A164.

[11] N. Post, J. Cain, K. McDonald, S. Case, J. Lesko, Residual strength prediction of composite materials: Random spectrum loading, Eng. Fract. Mech. 75 (2008) 2707–2724.

[12] J. Yang, D. Jones, S. Yang, A. Meskini, A stiffness degradation model for graphite/epoxy laminates, J. Compos. Mater. 24 (1990) 753–769.

[13] W. Hwang, K. Han, Fatigue of composites—Fatigue modulus concept and life prediction, J. Compos. Mater. 20 (1986) 154–165.

[14] A. Varvani-Farahani, H. Haftchenari, M. Panbechi, An energy-based fatigue damage parameter for off-axis unidirectional FRP composites, Compos. Struct. 79 (2007) 381–389.

[15] H. Krüger, R. Rolfes, A physically based fatigue damage model for fibre-reinforced plastics under plane loading, Int. J. Fatigue 70 (2015) 241–251.

[16] M. Brod, G. Just, A. Dean, E. Jansen, I. Koch, R. Rolfes, M. Gude, Numerical modelling and simulation of fatigue damage in carbon fibre reinforced plastics at different stress ratios, Thin-Walled Struct. 139 (2019) 219–231.

[17] I. Koch, G. Just, M. Brod, J. Chen, A. Doblies, A. Dean, M. Gude, R. Rolfes, C. Hopmann, B. Fiedler, Evaluation and modeling of the fatigue damage behavior of polymer composites at reversed cyclic loading, Materials 12 (2019).

[18] M. Brod, A. Dean, S. Scheffler, C. Gerendt, R. Rolfes, Numerical modeling and experimental validation of fatigue damage in cross-ply CFRP composites under inhomogeneous stress states, Composites B 200 (2020) 108050.

[19] C. Gerendt, A. Dean, T. Mahrholz, N. Englisch, S. Krause, R. Rolfes, On the progressive fatigue failure of mechanical composite joints: Numerical simulation and experimental validation, Compos. Struct. 248 (2020) 112488.

[20] M. Brod, A. Dean, R. Rolfes, Numerical life prediction of unidirectional fiber composites under block loading conditions using a progressive fatigue damage model, Int. J. Fatigue 147 (2021) 106159.

[21] A. Dean, S. Sahraee, K. Ozenc, J. Reinoso, M. Kaliske, R. Rolfes, A thermodynamically consistent framework to couple damage and plasticity microplane-based formulations for fracture modeling: development and algorithmic treatment, Int. J. Fract. 203 (2017) 115–134.

[22] J. Boldrini, E. Barros de Moraes, L. Chiarelli, F. Fumes, M. Bittencourt, A non-isothermal thermodynamically consistent phase field framework for structural damage and fatigue, Comput. Methods Appl. Mech. Engrg. 312 (2016) 395–427.

[23] C. Schreiber, R. Müller, C. Kuhn, Phase field simulation of fatigue crack propagation under complex load situations, Arch. Appl. Mech. 91 (2021) 563–577.

[24] P. Carrara, M. Ambati, R. Alessi, L. De Lorenzis, A framework to model the fatigue behavior of brittle materials based on a variational phase-field approach, Comput. Methods Appl. Mech. Engrg. 361 (2020) 112731.

[25] R. Alessi, V. Crismale, G. Orlando, Fatigue effects in elastic materials with variational damage models: A vanishing viscosity approach, J. Nonlinear Sci. 29 (2019) 1041–1094.

[26] K. Seleš, F. Aldakheel, Z. Tonković, J. Sorić, P. Wriggers, A general phase-field model for fatigue failure in brittle and ductile solids, Comput. Mech. 67 (2021) 1431–1452.

[27] M. Seiler, T. Linse, P. Hantschke, M. Kästner, An efficient phase-field model for fatigue fracture in ductile materials, Eng. Fract. Mech. 224 (2020) 106807.

[28] Z. Khalil, A.Y. Elghazouli, E. Martínez-Pañeda, A generalised phase field model for fatigue crack growth in elastic–plastic solids with an efficient monolithic solver, Comput. Methods Appl. Mech. Engrg. 388 (2022) 114286.

[29] R. Alessi, S. Vidoli, L. De Lorenzis, A phenomenological approach to fatigue with a variational phase-field model: The one-dimensional case, Eng. Fract. Mech. 190 (2018) 53–73.

[30] M. Simoes, E. Martínez-Pañeda, Phase field modelling of fracture and fatigue in shape memory alloys, Comput. Methods Appl. Mech. Engrg. 373 (2021) 113504.

[31] M.M. Hasan, T. Baxevanis, A phase-field model for low-cycle fatigue of brittle materials, Int. J. Fatigue 150 (2021) 106297.

[32] A. Golahmar, P.K. Kristensen, C.F. Niordson, E. Martínez-Pañeda, A phase field model for hydrogen-assisted fatigue, Int. J. Fatigue 154 (2022) 106521.

[33] J. Ulloa, J. Wambacq, R. Alessi, G. Degrande, S. François, Phase-field modeling of fatigue coupled to cyclic plasticity in an energetic formulation, Comput. Methods Appl. Mech. Engrg. 373 (2021) 113473.

[34] P.K. Kristensen, E. Martínez-Pañeda, Phase field fracture modelling using quasi-Newton methods and a new adaptive step scheme, Theor. Appl. Fract. Mech. 107 (2020) 102446.

[35] A. Golahmar, C.F. Niordson, E. Martínez-Pañeda, A phase field model for high-cycle fatigue: Total-life analysis, Int. J. Fatigue 170 (2023) 107558.

[36] F. Aldakheel, C. Schreiber, R. Müller, P. Wriggers, Phase-field modeling of fatigue crack propagation in brittle materials, in: Current Trends and Open Problems in Computational Mechanics, Springer International Publishing, Cham, ISBN: 978-3-030-87312-7, 2022, pp. 15–22.

[37] M. Harnau, K. Schweizerhof, About linear and quadratic "solid-shell" elements at large deformations, Comput. Struct. 80 (2002) 805–817.

[38] S. Klinkel, W. Wagner, A geometrical non-linear brick element based on the EAS-method, Internat. J. Numer. Methods Engrg. 40 (1997) 4529–4545.

[39] C. Miehe, A theoretical and computational model for isotropic elastoplastic stress analysis in shells at large strains, Comput. Methods Appl. Mech. Engrg. 155 (1998) 193–233.

[40] J. Reinoso, A. Blázquez, Application and finite element implementation of 7-parameter shell element for geometrically nonlinear analysis of layered CFRP composites, Compos. Struct. 139 (2016) 263–276.

[41] M. Schwarze, S. Reese, A reduced integration solid-shell finite element based on the EAS and the ANS concept—Large deformation problems, Internat. J. Numer. Methods Engrg. 85 (2011) 289–329.

[42] M. Bischoff, E. Ramm, Shear deformable shell elements for large strains and rotations, Internat. J. Numer. Methods Engrg. 40 (1997) 4427–4449.

[43] J. Korelc, P. Wriggers, Consistent gradient formulation for a stable enhanced strain method for large deformations, Eng. Comput. 13 (1996) 103–123.

[44] J. Simo, F. Armero, R. Taylor, Improved versions of assumed enhanced strain tri-linear elements for 3D finite deformation problems, Comput. Methods Appl. Mech. Engrg. 110 (1993) 359–386.

[45] J.C. Simo, M.S. Rifai, A class of mixed assumed strain methods and the method of incompatible modes, Internat. J. Numer. Methods Engrg. 29 (8) (1990) 1595–1638.

[46] R.A.F. Valente, R.M.N. Jorge, R.P.R. Cardoso, J.M.A. César de Sá, J.J.A. Grácio, On the use of an enhanced transverse shear strain shell element for problems involving large rotations, Comput. Mech. 30 (2003) 286–296.

[47] P. Betsch, E. Stein, An assumed strain approach avoiding artificial thickness straining for a non-linear 4-node shell element, Commun. Numer. Methods. Eng. 11 (1995) 899–909.

[48] E.N. Dvorkin, K.-J. Bathe, A continuum mechanics based four-node shell element for general non-linear analysis, Eng. Comput. 1 (1984) 77–88.

[49] J. Dolbow, N. Moës, T. Belytschko, Modeling fracture in Mindlin–Reissner plates with the extended finite element method, Int. J. Solids Struct. 37 (2000) 7161–7183.

[50] S. Natarajan, P. Baiz, S. Bordas, T. Rabczuk, P. Kerfriden, Natural frequencies of cracked functionally graded material plates by the extended finite element method, Compos. Struct. 93 (2011) 3082–3092.

[51] P.M.A. Areias, T. Belytschko, Non-linear analysis of shells with arbitrary evolving cracks using XFEM, Internat. J. Numer. Methods Engrg. 62 (2005) 384–415.

[52] P. Areias, J.-H. Song, T. Belytschko, Analysis of fracture in thin shells by overlapping paired elements, Comput. Methods Appl. Mech. Engrg. 195 (2006) 5343–5360.

[53] J. Kiendl, K.-U. Bletzinger, J. Linhard, R. Wüchner, Isogeometric shell analysis with Kirchhoff–Love elements, Comput. Methods Appl. Mech. Engrg. 198 (2009) 3902–3914.

[54] J. Kiendl, Y. Bazilevs, M.-C. Hsu, R. Wüchner, K.-U. Bletzinger, The bending strip method for isogeometric analysis of Kirchhoff–Love shell structures comprised of multiple patches, Comput. Methods Appl. Mech. Engrg. 199 (2010) 2403–2416.

[55] J. Kiendl, M.-C. Hsu, M.C. Wu, A. Reali, Isogeometric Kirchhoff–Love shell formulations for general hyperelastic materials, Comput. Methods Appl. Mech. Engrg. 291 (2015) 280–303.

[56] S. Forest, Micromorphic approach for gradient elasticity, viscoplasticity, and damage, J. Eng. Mech. 135 (2009) 117–131.

[57] T. Waffenschmidt, C. Polindara, A. Menzel, S. Blanco, A gradient-enhanced large-deformation continuum damage model for fibre-reinforced materials, Comput. Methods Appl. Mech. Engrg. 268 (2014) 801–842.

[58] R.H.J. Peerlings, R. De Borst, W.A.M. Brekelmans, J.H.P. De Vree, Gradient enhanced damage for quasi-brittle materials, Internat. J. Numer. Methods Engrg. 39 (1996) 3391–3403.

[59] S.S. Shishvan, S. Assadpour-asl, E. Martínez-Pañeda, A mechanism-based gradient damage model for metallic fracture, Eng. Fract. Mech. 255 (2021) 107927.

[60] P.K.A.V. Kumar, A. Dean, S. Sahraee, J. Reinoso, M. Paggi, Non-linear thermoelastic analysis of thin-walled structures with cohesive-like interfaces relying on the solid shell concept, Finite Elem. Anal. Des. 202 (2022) 103696.

[61] P.K. Asur Vijaya Kumar, A. Dean, J. Reinoso, M. Paggi, Nonlinear thermo-elastic phase-field fracture of thin-walled structures relying on solid shell concepts, Comput. Methods Appl. Mech. Engrg. 396 (2022) 115096.

[62] P.K. Asur Vijaya Kumar, A. Dean, J. Reinoso, M. Paggi, Thermo-elastic solid shell formulation with phase field fracture for thin-walled FGMs, Thin-Walled Struct. 179 (2022) 109535.

[63] J. Reinoso, M. Paggi, C. Linder, Phase field modeling of brittle fracture for enhanced assumed strain shells at large deformations: formulation and finite element implementation, Comput. Mech. 59 (2017) 981–1001.

[64] M. Ambati, T. Gerasimov, De Lorenzis, A review on phase-field models of brittle fracture and a new fast hybrid formulation, Comput. Mech. 1 (2015) 383–405.

[65] C. Kuhn, R. Müller, A new finite element technique for a phase field model of brittle fracture, J. Theoret. Appl. Mech. 49 (2011) 1115–1133.

[66] C. Miehe, M. Hofacker, F. Welschinger, A phase field model for rate-independent crack propagation: Robust algorithmic implementation based on operator splits, Comput. Methods Appl. Mech. Engrg. 199 (2010) 2765–2778.

[67] C. Miehe, F. Welschinger, M. Hofacker, Thermodynamically consistent phase-field models of fracture: Variational principles and multi-field FE implementations, Internat. J. Numer. Methods Engrg. 83 (2010) 1273–1311.

[68] C. Steinke, K. Özenç, G. Chinaryan, M. Kaliske, A comparative study of the r-adaptive material force approach and the phase-field method in dynamic fracture, Int. J. Fract. 201 (2016) 97–118.

[69] C. Steinke, M. Kaliske, A phase-field crack model based on directional stress decomposition, Comput. Mech. 63 (2019) 1019–1046.

[70] P. Asur Vijaya Kumar, A. Dean, J. Reinoso, P. Lenarda, M. Paggi, Phase field modeling of fracture in functionally graded materials: Gamma-convergence and mechanical insight on the effect of grading, Thin-Walled Struct. 159 (2021) 107234.

[71] A. Dean, P. Asur Vijaya Kumar, J. Reinoso, C. Gerendt, M. Paggi, E. Mahdi, R. Rolfes, A multi phase-field fracture model for long fiber reinforced composites based on the puck theory of failure, Compos. Struct. 251 (2020) 112446.

[72] B. Kötter, J. Endres, J. Körbelin, F. Bittner, H.-J. Endres, B. Fiedler, Fatigue and fatigue after impact behaviour of thin- and thick-ply composites observed by computed tomography, Composites C 5 (2021) 100139.

[73] A. Mitrou, A. Arteiro, J. Reinoso, P.P. Camanho, Modeling fracture of multidirectional thin-ply laminates using an anisotropic phase field formulation at the macro-scale, Int. J. Solids Struct. 273 (2023) 112221.

[74] L. Ambrosio, A. Braides, Energies in SBV and variational models in fracture mechanics, in: D. Cioranescu, A. Damlamian, P. Donato (Eds.), Homogenization and Applications to Material Sciences, GAKUTO, Gakkotosho, Tokio, Japan, 1997, pp. 1–22.

[75] B. Bourdin, G. Francfort, J.-J. Marigo, Numerical experiments in revisited brittle fracture, J. Mech. Phys. Solids 48 (2000) 797–826.

[76] A. Jaubert, J.J. Marigo, Justification of Paris-type fatigue laws from cohesive forces model via a variational approach, Contin. Mech. Thermodyn. 18 (2006) 23–45.